Chapter 9

Solar Membrane Distillation: Use of a Helically Coiled Fiber

Adel Zrelli

Additional information is available at the end of the chapter

http://dx.doi.org/10.5772/67653

Abstract

Membrane distillation (MD) is a novel process introduced to overcome the disadvantages of the conventional distillation process. MD has gained much interest, principally, for its lower energy demand and higher rejection factors. Many configurations of the membrane module have been tested to improve the MD process. In this case, and in order to see the possibility of using the helically coiled fiber for MD coupled with solar energy, a mathematical model has been developed. This model describes the evolutions of permeate flow rate with the variation of inlet feed characteristics, solar flux, and so on. A comparison between the use of linear and helically-coiled fiber shows an enhancement of the temperature polarization coefficient about 6% for the case of the helical fiber and to have an improvement factor by 28%. For the case of the effect of solar energy on the permeate flow rate, an increase of 264% is remarked for the variation of the direct solar flux from 200 to 800 W/m^2. However, a reduction of 12% for the permeate flux is obtained, when the inlet feed concentration grows from 10 to 300 g/l.

Keywords: Vacuum membrane distillation, Solar energy, Helical fiber, Simulation

1. Introduction

Water is abundant on Earth. The majority (97.2%) consists of seawater [1]. The rest is composed of 2.2% ice caps and glaciers (unusable directly), while fresh water, which is found in lakes, rivers, and groundwater, is only 0.6% [2]. In addition, the distribution of this water is very uneven. In fact, only 10 countries share 60% of freshwater reserves while 29 countries are facing a shortage of fresh water. These countries are located in Africa and the Middle East [3]. However, these freshwater may not be potable. Allowing this globally, many countries are below the threshold shortage of drinking water. The drinking water is a major issue for

development and survival for humans [4]. This shortage is a result of poor management of reserves, water pollution, and population growth. Also, this water shortage affects nearly 80% of world's population [5]. To overcome this shortage of drinking water, several solutions were presented among which are the desalination of brackish water or seawater. Mainly, the desalination technologies, used around the world, are the thermal with 33% of total capacity and membrane processes with 56% of total capacity [6]. The first type, thermal processes, is based on physical change in the water state. For this type, the two techniques, which gained great global interest to offer to yet effective solutions to desalinate water, are multistage flash distillation (MSF) and multi-effect distillation (MED) [7]. For the second type, which is the membrane processes, a membrane is used to separate the water from the saline water (brackish or seawater). In this case, the characteristics of the membrane (such as porosity, wettability, selectivity, electric charge, etc.) are so important in order to obtain a high efficiency for the membrane processes. The two main techniques, used in this type, are the reverse osmosis (RO) and the electrodialysis (ED) [6]. Each technique uses the ability of membranes to separate selectively salts and water from the saline water. These two types of desalination technologies (thermal and membrane processes) have a high-energy demand, and the process performance is limited by the osmotic pressure or concentration polarization. In order to overcome these drawbacks, a promising alternative technology for desalination is introduced, which is the membrane distillation (MD) due principally to lower energy cost and membrane fouling [8]. MD is composed of four configurations. These configurations are the direct contact membrane distillation (DCMD), the air gap membrane distillation (AGMD), the sweeping gas membrane distillation (SGMD), and the vacuum membrane distillation (VMD) [9]. VMD has attracted increasing interest for various applications. From energy consumption point of view, it could clearly compete with reverse osmosis, when coupled with alternate source of energy such as solar energy [10]. In order to couple VMD to solar energy, different configurations can be used. In this case, membrane can be placed in or out of the absorber of the solar collector. Furthermore, many configurations of the hollow fiber membrane can be used. Among these configurations, we found the linear and the helical fibers.

In this chapter, a brief outline of the main thermal and membrane desalination processes will be presented. This will be followed by the exposure of the membrane distillation and its different configurations and the used hollow fiber geometries in order to increase the process performance. Therefore, this chapter attempts to develop a novel hollow fiber module design, which is the helically coiled fiber. A comparison of the performance of the helically coiled hollow fiber to those of linear fiber will be done. The effects of this novel configuration on the permeate flow rate and the temperature polarization coefficient will be highlighted. In addition, the effects of the process conditions, such as the initial feed concentration and the solar radiation, on the permeate flow rate will be evaluated.

2. Desalination processes

The most important desalination processes are the thermal processes and membrane processes.

http://dx.doi.org/10.5772/67653

2.1. Thermal processes

2.1.1. Multi-effect distillation (MED)

These processes are composed principally of multistage flash (MSF) and multi-effect distillation (MED). MED is the oldest technique applied for seawater desalination [11]. The MED principle is based on heat transfer from the condensing steam to feed seawater or brine in a series of effects (**Figure 1**). In this case, the steam produced in the first effect was condensed to produce fresh water in the second effect. This latter effect was operated at slightly lower pressure and temperature than in the previous effect. The heat of steam condensation allows to evaporate a portion of the seawater contained in the second effect and so on. Thus, only the energy required for the evaporation in the first effect is of external origin. MED can work with a low steam temperature as heat source (70–80°C) and the multiplication of effects allows to reduce the specific consumption. Therefore, the number of effects is usually between 8 and 16 [12, 13].

2.1.2. Multistage flash (MSF)

The MSF process comes in practice since the late 1950s [15]. The distillation was done, in this case, in a series of flash chambers. The generation of steam, from brackish water or seawater, was the result of a pressure drop and not of heat exchange with condensing steam, which is the case of MED. The principle is so simple, the brackish water or seawater was pressurized and heated to the plant's maximum allowable temperature (limited to about 110°C). Afterwards, this heated liquid was introduced into a chamber maintained at slightly below the saturation vapor pressure of the water (**Figure 2**). This chamber pressure level induces the flash of a fraction of its water content into steam. This latter is converted into fresh water by condensation on heat exchanger with a series of closed pipes, while the rest of the heated liquid continues flowing through a series of chambers. The number of chambers, for this technology, is between 20 and 25 [11, 14, 16].

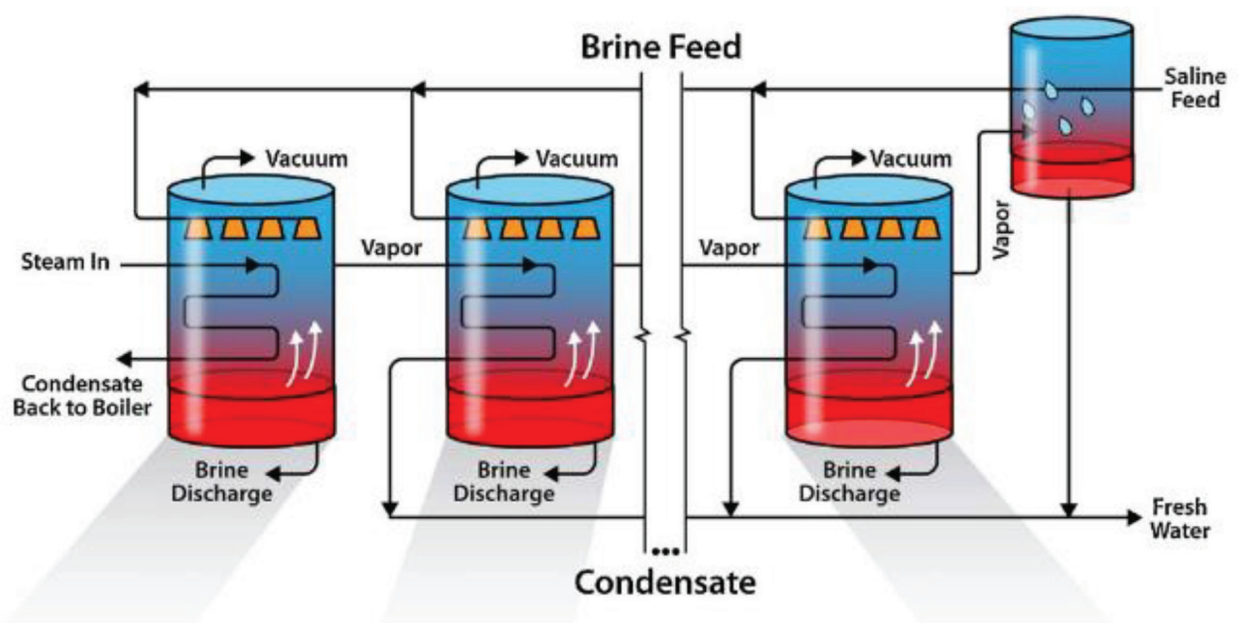

Figure 1. Diagram of a multi-effect desalination (MED) unit [14].

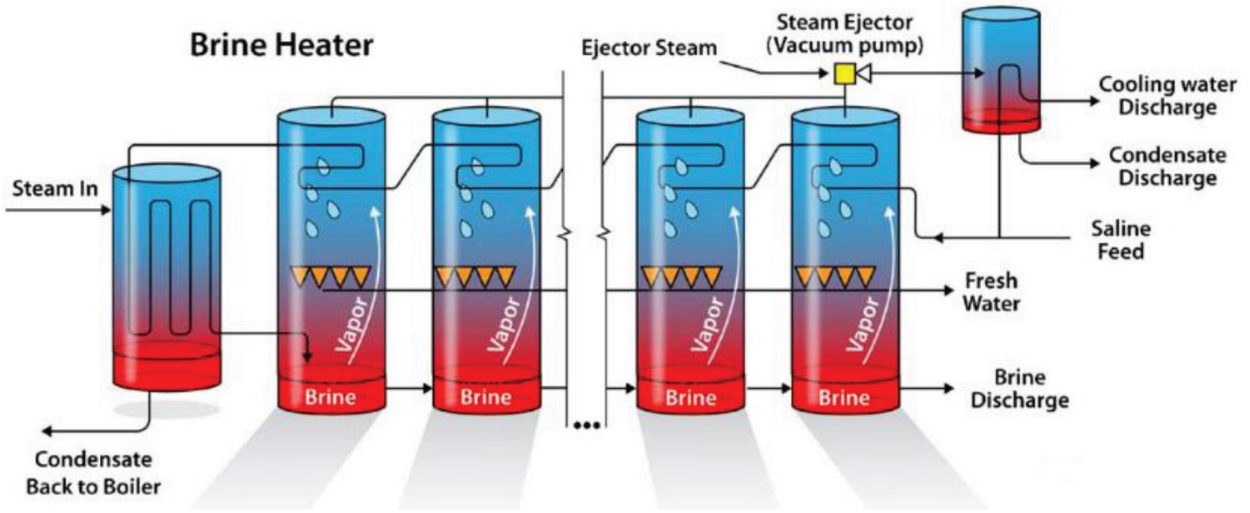

Figure 2. Diagram of a multistage flash distillation (MSF) unit [14].

2.2. Membrane processes

Membrane processes include electrodialysis (ED) and reverse osmosis (RO) [17].

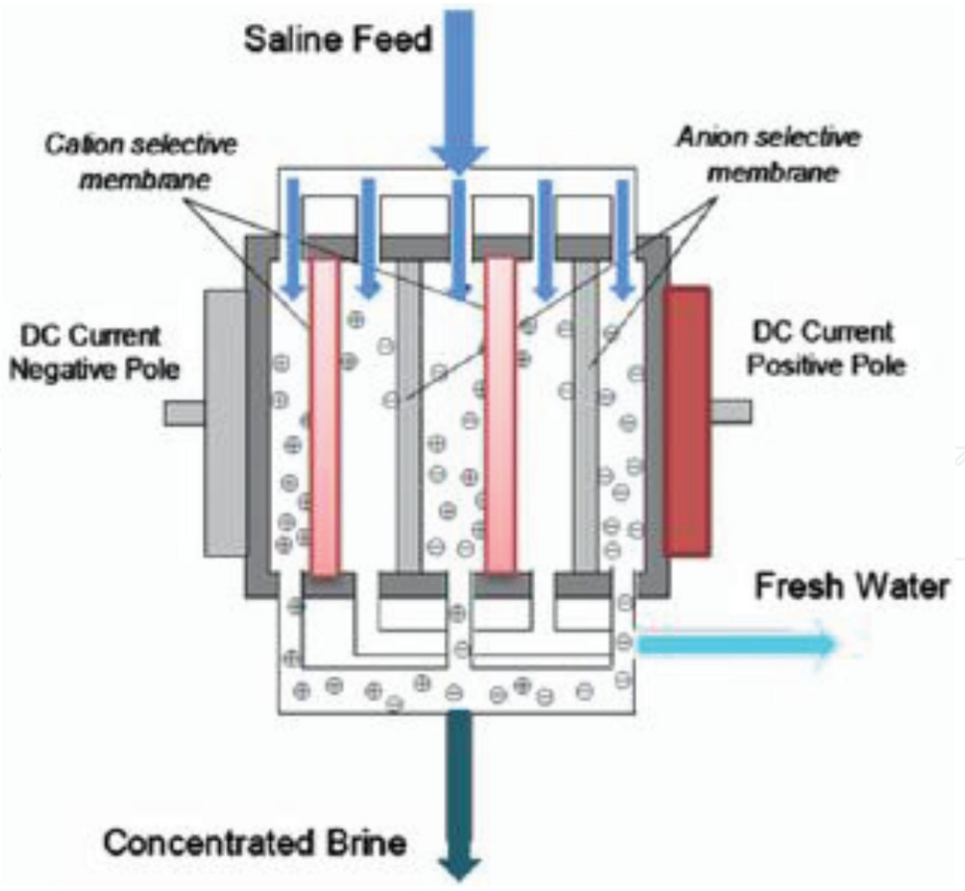

Figure 3. Schematic diagram of electrodialysis desalination process [14].

2.2.1. Electrodialysis

Electrodialysis process (ED) is an electrochemical separation process, which has been in commercial use for desalination of brackish water since 1970s, particularly for small- and medium-scale processes. This process uses the electric direct current to remove the salt ions in the brackish water. The latter passes between pairs of anion-exchange and cation-exchange membranes. The cations (positive ions) migrate from the brackish water toward the negative electrode through the cation-exchange membranes, which allow only cations to pass (**Figure 3**). On the other hand, the anions (negative ions) migrate toward the anode through the anion-exchange membranes. In a conventional process, a large number of alternating cation-exchange and anion-exchange membranes are stacked together, separated by flow spacers, which are plastic sheets that allow the passage of water. The total power consumption of ED units ranges from 0.7 to 2.5 kWh/m^3 of desalinated water for feed water salinity of 2500 ppm and from 2.64 to 5.5 kWh/m^3 of desalinated water for feed water salinity of 5000 ppm [18–20].

2.2.2. Reverse osmosis

Reverse osmosis (RO) is a pressure-driven process that separates two solutions with different concentrations across a semi-permeable membrane (**Figure 4**). The rate of fresh water that penetrates the membrane depends on the difference between the applied pressure and the osmotic pressure of the feed salt water. The osmotic pressure is directly related to the salt concentration in the saline water. For brackish water desalination, the operating pressures range from 18 to 28 bar, and for seawater desalination from 55 to 69 bar [21]. The discharge

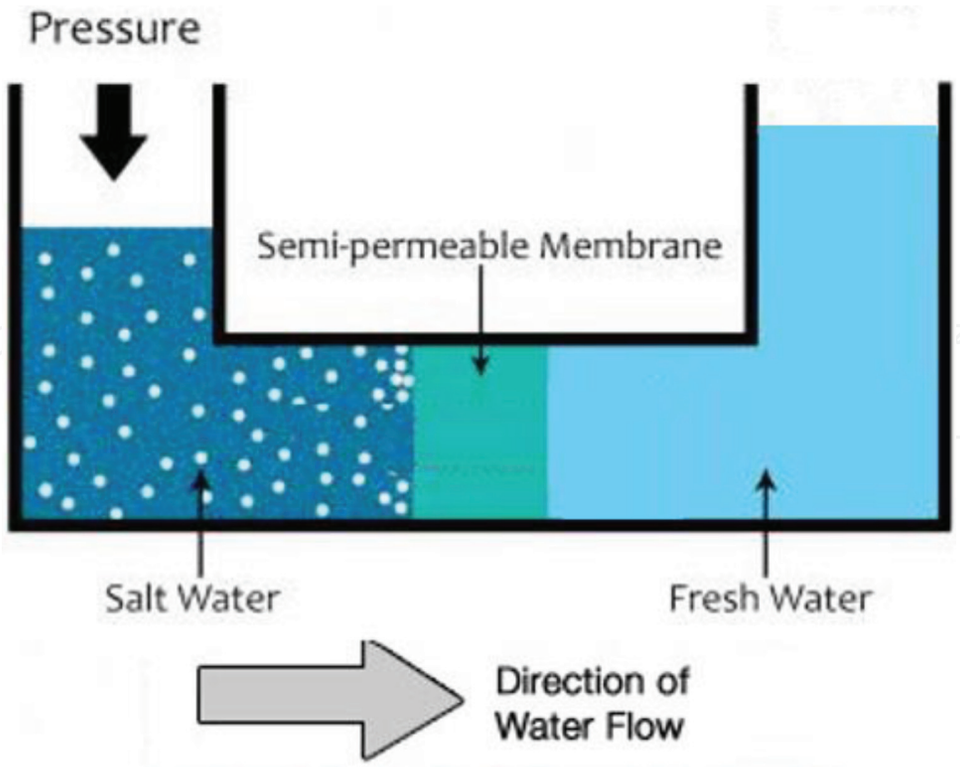

Figure 4. Schematic diagram of RO desalination process.

brine from an RO unit ranges from 20 to 70% of the flow feed water, depending on salinity of the feed water, applied pressure, and type of membrane.

Until today, the predominant desalination processes in use are RO and MSF, which constitute 53 and 25% of worldwide capacity, respectively (**Figure 5**). However, these processes have some disadvantages, which are described in the subsequent text.

They are considered energy intensive either by the heat demand for the MSF process (generally for the thermal processes) or by the high-pressure demand as in reverse osmosis. The used pressure for the RO process is about 10–15 bar for brackish water and 50–80 bar for seawater, and the consumed electrical energy, to produce 1 m^3 of desalinated water, is in the range of 3–4 kWh [23]. This high-energy consumption contributes to further environmental problems such as more pollutants and undesired emissions. Other disadvantages of these processes are the high maintenance cost of the mechanical equipment and the limited membrane lifespan [24]. Also, reverse osmosis efficiency is strongly affected by the osmotic pressure of the highly concentrate feed solutions, which imply the use of high pressure and the reduction of the salt rejection with the decay by 50% of permeate flux [25]. These drawbacks push down the efficiency of those processes, which require the search for alternative, environment friendly, and sustainable desalination.

2.3. Membrane distillation

2.3.1. Membrane distillation principle

Membrane distillation (MD) is an alternative to the traditional evaporative distillation systems used for desalination or water purification processes. MD is a thermally driven membrane process developed over the last 60 years [26]. In this process, a hydrophobic microporous membrane separates a hot and cold stream (**Figure 6**). This membrane serves, also, as a physical support for vapor transport but a barrier to liquid penetration, thus allowing the separation of volatile and non-volatile species. In the case of salty water, the water (volatile

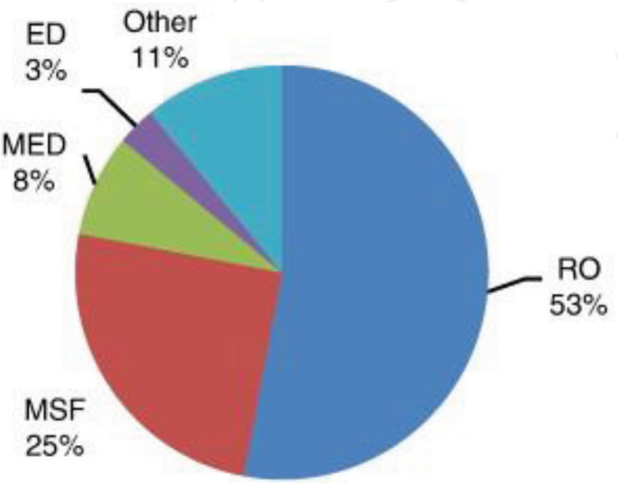

Figure 5. Distribution of plant capacity according to desalination process [6, 22].

http://dx.doi.org/10.5772/67653

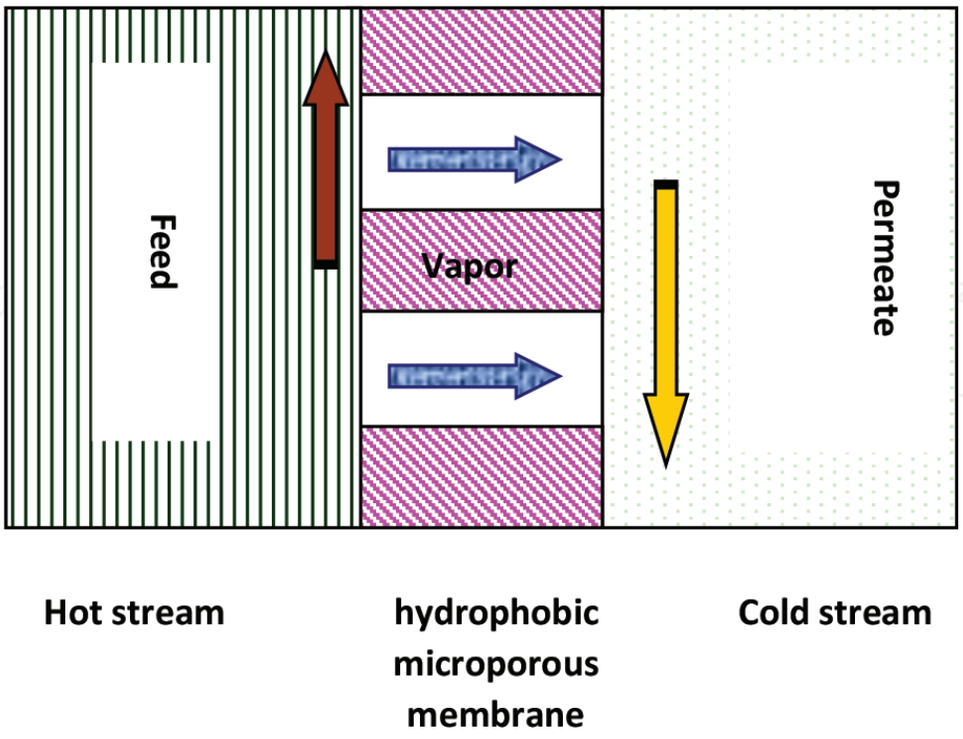

Figure 6. Principle of membrane distillation.

specie) passes through the membrane as vapor without salt and condenses on the low-temperature side and distillate is formed [27, 28].

Some of advantages of MD processes over conventional desalination processes such as MSF and RO are as follows:

- Lower working temperature, which leads to coupled MD to low-grade and renewable energy source such as solar energy.
- Lower operating pressures, which induce a less demanding membrane mechanical properties.
- Outstanding rejection performance, of non-volatile solute, which can reach as high as 100%.
- Performance is not significantly affected by high osmotic pressure or concentration polarization because the solution vapor pressure changes only marginally with salt concentration.
- Reduced chemical interaction between membrane and process solution [8, 25, 27, 29, 30].

2.3.2. MD configurations

MD can be classified into four different configurations according to the nature of the cold side of the membrane [31]: the first configuration is the direct contact membrane distillation (DCMD) in which the membrane is in direct contact with liquid phases on both sides. The volatile components of the feed evaporate at the interface feed/membrane diffuse through the

membrane pores and condensate at the cold side in the distillate stream [26–29]. The second configuration is air gap membrane distillation (AGMD) in which an air gap is interposed between the membrane and the condensate surface. This stagnant air gap reduces heat losses due to conduction, thus increasing the thermal efficiency of this configuration [32]. The sweeping gas membrane distillation (SGMD) represents the third configuration. In this configuration, a cold inert gas is used in permeate side as carrier for the produced vapor. The condensation of this vapor takes place outside the membrane module [8]. The fourth and the last configuration is the vacuum membrane distillation (VMD), in which the vapor phase is vacuumed from the liquid through the membrane and condensed outside of the membrane module [30].

VMD presents many advantages when compared to the other MD configurations by presenting the highest flux and desalination rate, and the lowest fresh water conductivity (**Figures 7** and **8**). For VMD, the two main advantages are a very low conductive heat loss and a reduced mass transfer resistance [30, 33–35].

2.3.3. Coupling MD with solar energy

Generally, desalination consumes much energy. In order to minimize the energy usage and consequently the cost, the use of renewable energy (wind, geothermal, solar, etc.) is a feasible and potential solution. In addition, the lack of drinkable water often accompanies the abundance of solar radiation, which makes favorable the coupling of the desalination processes with the solar energy [36]. In the case of VMD, the permeate flux could be enhanced, when it is coupled with solar energy, and its value can be increased from the range of (5–15 l/h m^2) to that (40–85 l/h m^2). Following this coupling of VMD with solar energy, this MD process could clearly compete with RO [37].

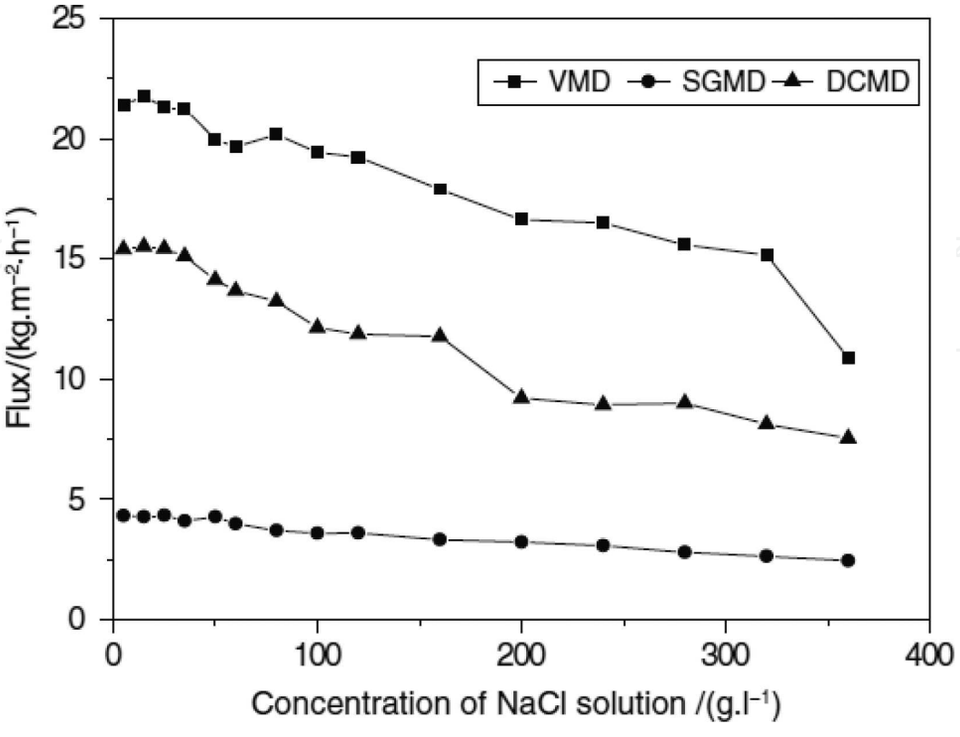

Figure 7. Comparison of flux for three configurations at different feed concentration [33].

http://dx.doi.org/10.5772/67653

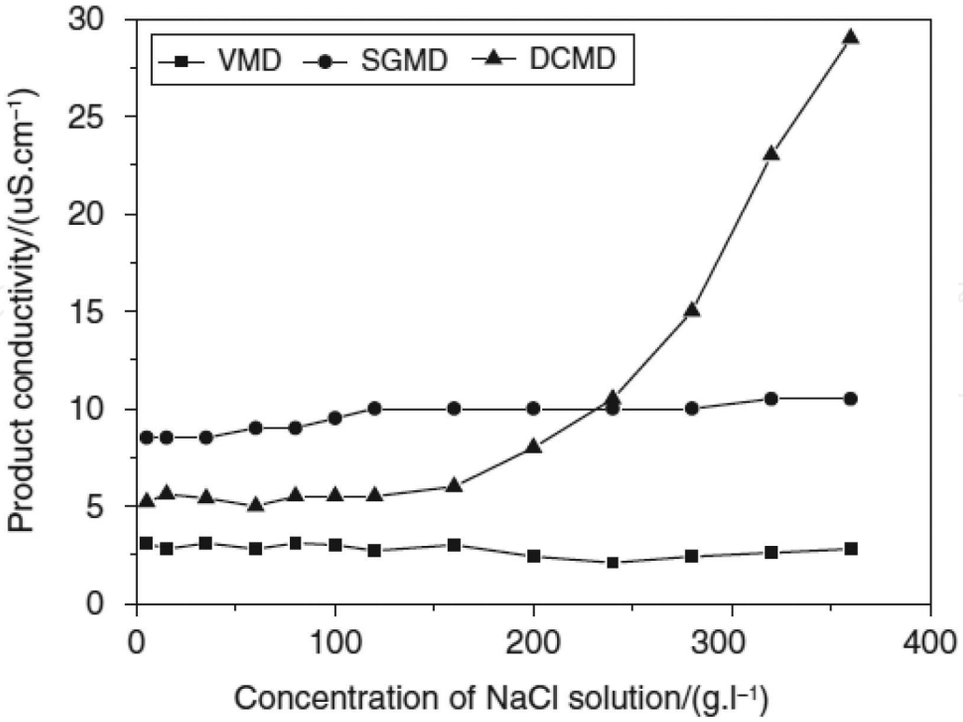

Figure 8. Comparison of conductivity for three configurations at different feed concentration [33].

2.3.4. Module geometry configurations

In MD process, the most studied geometry configurations are flat sheet and hollow fiber membrane modules. The hollow fiber membrane modules are preferable due to their larger membrane area per unit volume and highest packing density of all module types and modular versatility. The hollow fiber packing density is about 3000 m^2/m^3 [8]. However, a poor configuration of hollow fiber modules will result in the reduction of the permeate production and the efficiency of the MD process. In order to overcome this problem, many studies have focused on strategies to improve the MD performance through designing novel membrane modules [38–41] and enhancing the permeate flux. In this case, the introduction of baffles (**Figure 9**), in

Figure 9. Hollow fiber module with window baffles [38].

membrane module, provides a better flow distribution and could increase the shell-side heat-transfer coefficients leading to 20–28% flux enhancement.

Furthermore, the use of hollow fiber configurations with wavy geometries (twisted and braided (**Figure 10**)) led to flux enhancements as high as 36%.

Yang et al. [39] reported that the greatest enhancement is achieved by the modules with spacer-knitted (**Figure 11**) for which the flux is increased more than 90% when compared with the randomly packed module. For the same configuration (spacer-knitted) and when the operating conditions were modified, the flux enhancement achieved was only 51.8% [41].

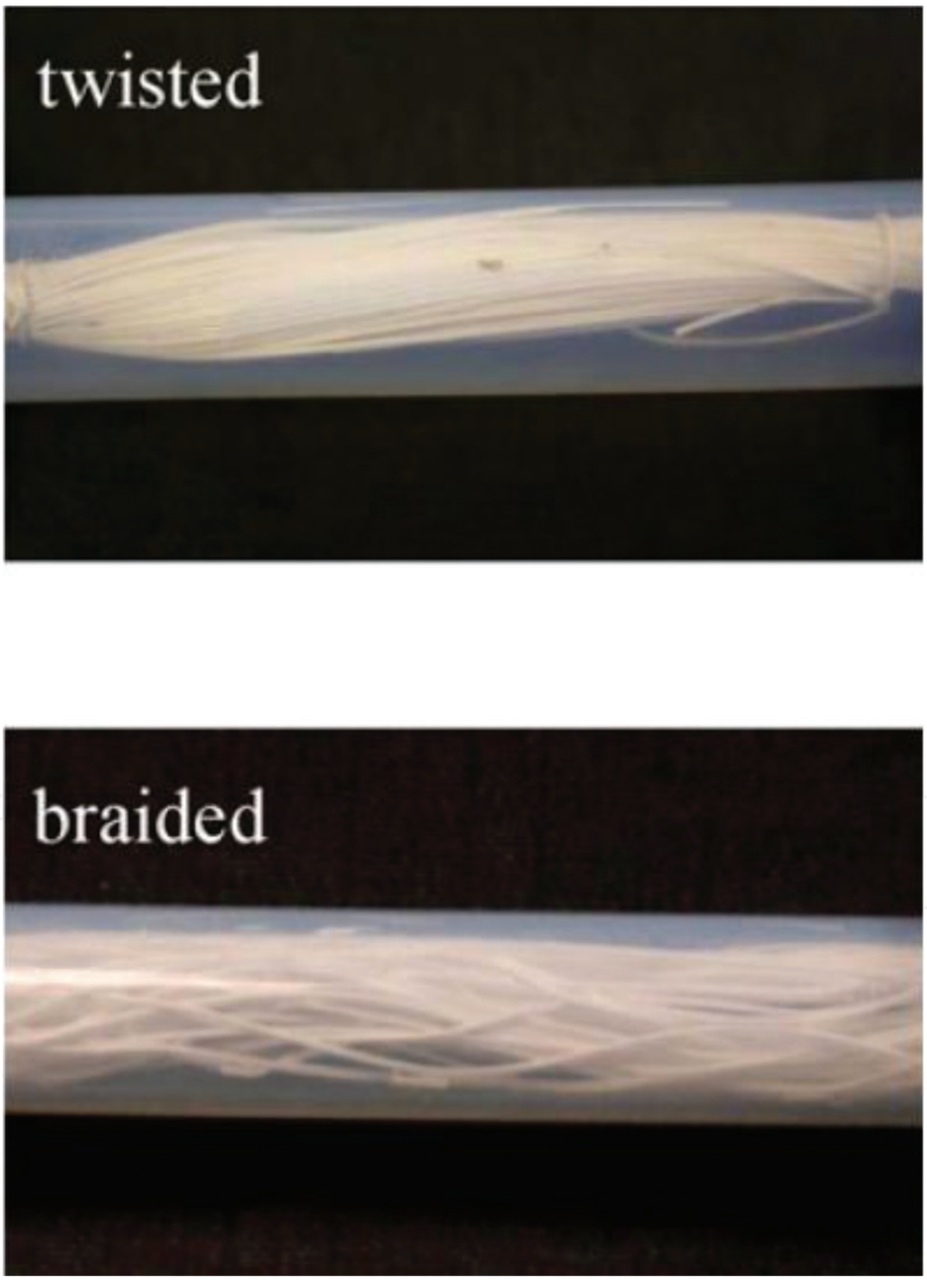

Figure 10. Wavy geometries (twisted and braided) hollow fiber module [38].

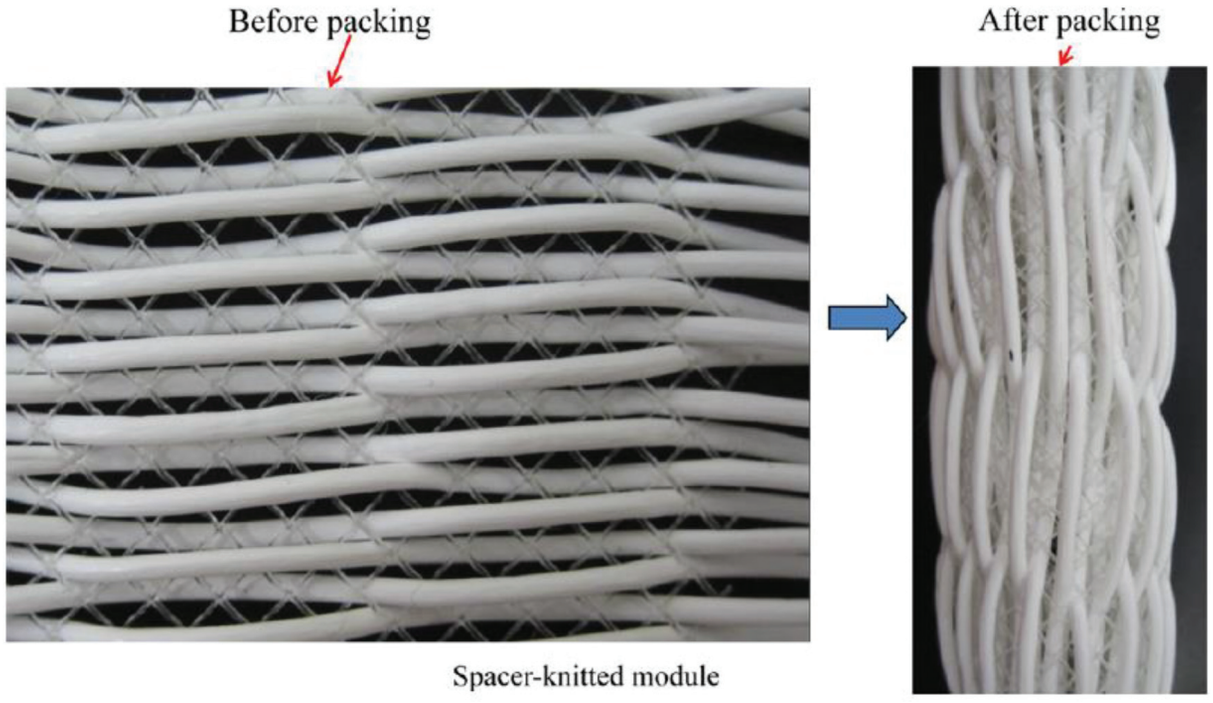

Figure 11. Spacer-knitted design of hollow fiber module [39].

On the other hand, the other fiber configuration is the helically coiled fiber. Few studies have been undertaken on the use of this configuration. Among these studies, we present the Mallubhota et al. study [42]. In this work, a comparison, for nanofiltration, between linear and helical modules was done. The results show an enhancement of the permeation rate during their use of the helical module. This enhancement is due to the reduction membrane fouling and polarization concentration. In addition, when the helical-coiled fiber was used by Nagase et al. [43], an enhancement in the mass transfer coefficient and consequently in the permeate rate has been observed. The same finding has been proved by Liu et al. when they used this helical configuration in membrane extraction.

3. Use of helically coiled fiber

3.1. Design description

In our case, the solar desalination installation (shown in **Figure 12**) is composed of parabolic trough concentrator. At the focal axis, the absorber is mounted, which is in the shape of a cylindrical tube. This absorber contains the hollow fiber membrane. This membrane has the shape of a coil and the configuration of an absorber, and the membrane is similar to a helically coiled heat exchanger. In addition to that, solar rays are focused into the absorber, and an increase of the feed temperature is consequently reported.

In order to have a symmetrical conception, we study a system that contains two helically coiled fibers (**Figure 13**). Since the flow is symmetric about a vertical plane passing through the axis of the cylinder, only the half-plane needs to be considered (**Figure 14**).

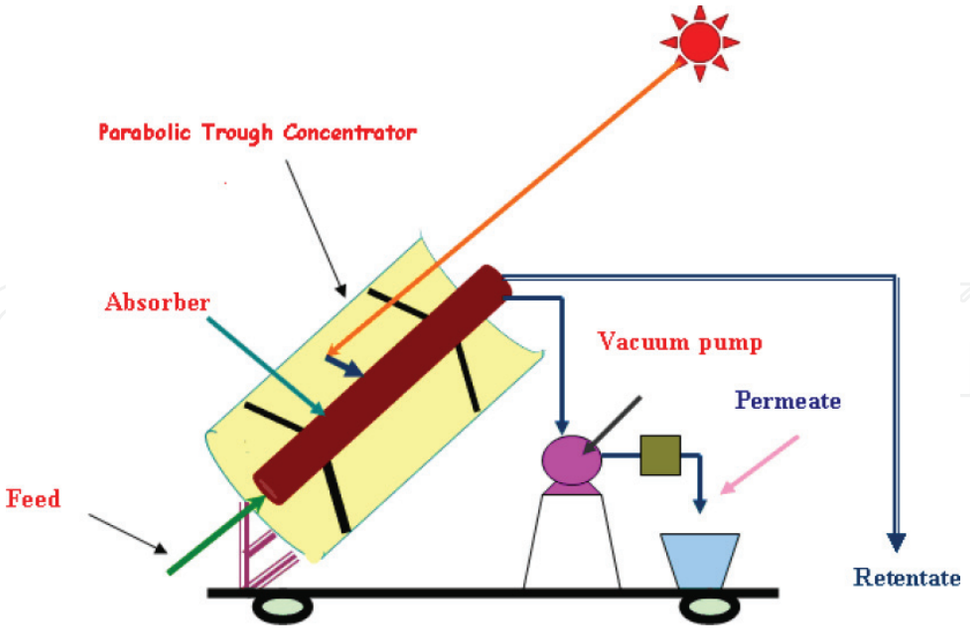

Figure 12. Solar-VMD installation.

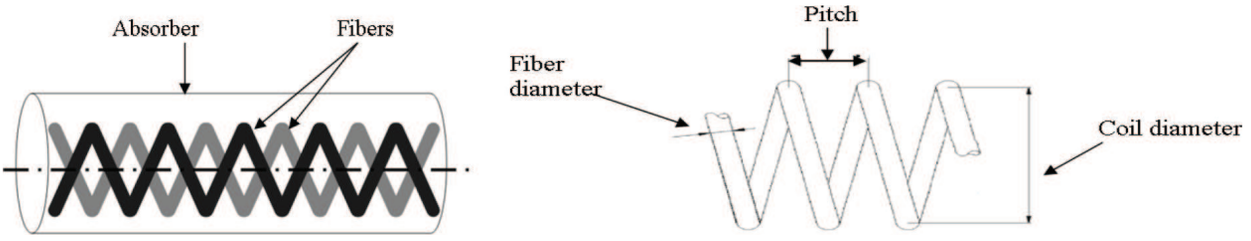

Figure 13. Basic geometry of a helical fiber.

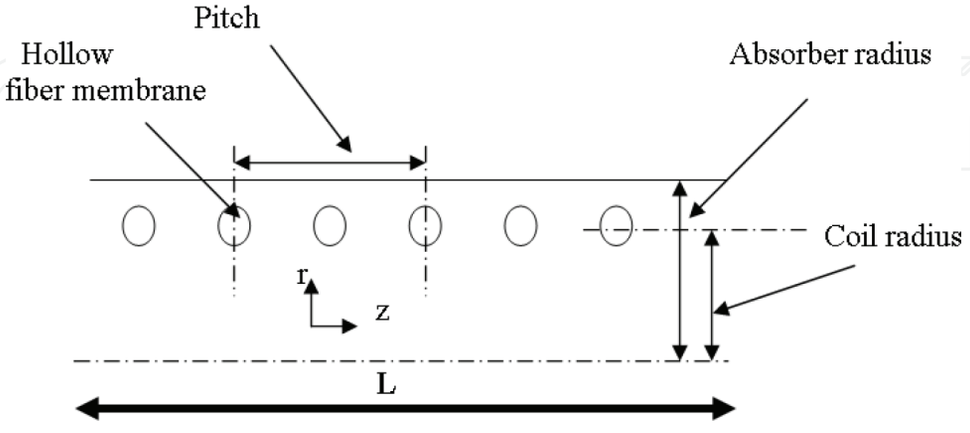

Figure 14. Domain of study [44].

3.2. Mathematical model

Based on **Figures 13** and **14**, we developed a mathematical model and the following assumptions are used for the numerical calculations:

1. The flow is fully developed before it enters the inlet of the absorber.
2. Fluid is incompressible and Newtonian.
3. The motion is considered as axisymmetric, hence, only half of the absorber is considered.
4. The gravity force is neglected.
5. All angular gradient parameters are negligible; the model is described in the coordinates r and z.
6. No slip condition is valid on the surface of the fiber.
7. All simulations are carried out assuming steady state.

Under these conditions, the appropriate governing equations are written [45]:

Continuity equation:

$$\frac{\partial u_r}{\partial r} + \frac{u_r}{r} + \frac{\partial u_z}{\partial z} = 0 \tag{1}$$

Momentum equations:

$$u_r \frac{\partial u_r}{\partial r} + u_z \frac{\partial u_r}{\partial z} = \nu \left[\frac{\partial}{\partial r} \left(\frac{1}{r} \frac{\partial r u_r}{\partial r} \right) + \frac{\partial^2 u_r}{\partial z^2} \right] \tag{2}$$

$$u_r \frac{\partial u_z}{\partial r} + u_z \frac{\partial u_z}{\partial z} = -\frac{1}{\rho} \frac{\partial P}{\partial z} + \nu \left[\frac{1}{r} \frac{\partial}{\partial r} \left(\frac{r \partial u_z}{\partial r} \right) + \frac{\partial^2 u_z}{\partial z^2} \right] \tag{3}$$

Energy equation:

$$u_r \frac{\partial T}{\partial r} + u_z \frac{\partial T}{\partial z} = \alpha \left[\frac{1}{r} \frac{\partial}{\partial r} \left(r \frac{\partial T}{\partial r} \right) + \frac{\partial^2 T}{\partial z^2} \right] \tag{4}$$

The boundary conditions for velocity and temperature are as follows:

At the inlet of absorber, $Z = 0$:

$$\begin{aligned} u_z &= 2u_0 \left(1 - \left(\tfrac{r}{R} \right)^2 \right) \\ u_r &= 0 \\ T &= T_{in} \end{aligned} \tag{5}$$

At the exit, $Z = L$:

$$u_r = \frac{\partial u_z}{\partial z} = \frac{\partial T}{\partial z} = 0 \tag{6}$$

At the hollow fiber membrane surface:

$$\begin{aligned} u_z &= 0 \\ u_r &= 0 \\ T &= T_{\text{inter}} \end{aligned} \tag{7}$$

At the absorber interior wall, $r = R$:

$$\begin{aligned} u_z &= 0 \\ u_r &= 0 \\ T &= T_w \end{aligned} \tag{8}$$

The temperature at the feed/membrane interface (T_{inter}) is related to the bulk temperature (T_b) by the following heat balance equation [46]:

$$J_v L_v = h_f (T_b - T_{\text{inter}}) \tag{9}$$

The latent heat of vaporization of water (L_v) is given by [47]

$$L_v = 2538.2 - 2.91\ T_{\text{inter}} \tag{10}$$

The absorber interior wall temperature (T_w) is given by the below equation:

$$T_w = T_e - \frac{q_u e}{\lambda_m} \tag{11}$$

where T_e is the absorber exterior wall temperature and q_u is the useful heat flow, given by

$$q_u = q_a - q_e \tag{12}$$

The incident power of the absorber radiance, "q_a," is expressed by

$$q_a = IC_g \rho \gamma \alpha \tau \tag{13}$$

The sum of the heat losses by convection and radiation between the absorber and the surrounding, "q_e," is given by

$$q_e = \varepsilon_a \sigma ({T_e}^4 - (T_a - 11)^4) + (5.7 + 3.8 w_s)(T_e - T_a) \tag{14}$$

The thermal energy balance equation of the absorber "i" element (**Figure 15**) is

$$q_u s_i = \dot{m}_{oi} cp T_{foi} - \dot{m}_{ii} cp T_{fii} + (\dot{m}_{ii} - \dot{m}_{oi}) L_v \tag{15}$$

The dominant mechanism of mass transfer through the membrane pores at low vacuum

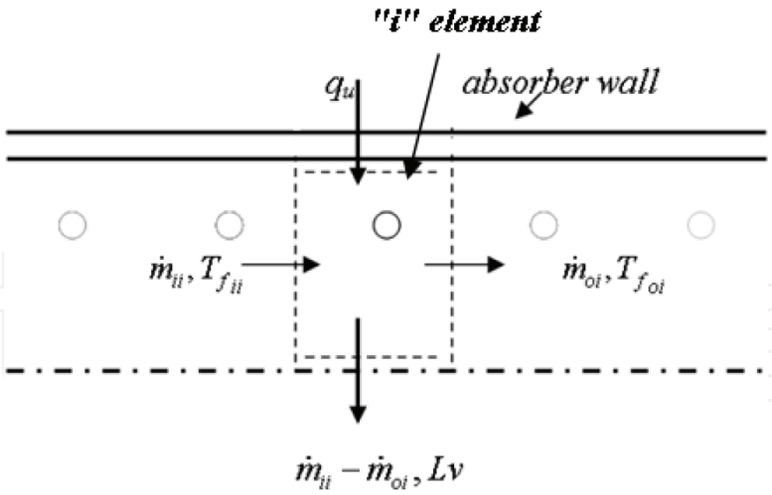

Figure 15. Thermal balance on the "*i*" element of the absorber [44].

pressures is Knudsen [48, 49]. This model suggests a linear relationship between the permeate flux (J_v) and the transmembrane water vapor pressure difference (ΔP) [10]:

$$J_V = \frac{k_m}{\sqrt{M_w}} \Delta P = \frac{k_m}{\sqrt{M_w}} (P_{\text{inter}} - P_v) \tag{16}$$

The membrane permeability coefficient (k_m) can be related to membrane structural properties such as its membrane thickness (δ), pore tortuosity (τ), and pore radius (r) [50]:

$$k_m = 1.064 \frac{r\varepsilon}{\delta\tau} \sqrt{\frac{1}{RT}} \tag{17}$$

The water vapor pressure (P_{inter}) at the liquid/vapor interface may be related with the temperature, by using Antoine's equation [51]:

$$P_{\text{inter}}(T) = \exp\left(23.238 - \frac{3841}{T - 45}\right) \tag{18}$$

where P_{inter} (T) is in Pa and T is in K.

Following an analogy between the helically coiled fiber and the coiled tube heat exchanger, we used the correlation presented by Salimpour [52, 53], in order to calculate the outside heat transfer coefficient

$$Nu = 19.64 \text{Re}^{0.513} \text{Pr}^{0.129} \gamma^{0.938} \tag{19}$$

$$\gamma = \frac{P}{2\pi R_c} \tag{20}$$

The helically coil length (Lc) is given by

$$Lc = \left(\frac{L+P}{P}\right)\sqrt{p^2 + (\pi Dc)^2} \tag{21}$$

For each "i" element of the absorber, we can calculate the permeate flow rate "$\dot{m}_{pi}$" according to the below equation:

$$\dot{m}_{pi} = J_{vi}\pi Lc_i d_o \tag{22}$$

The temperature polarization coefficient, TPC, is defined to measure the effective temperature difference between T_a and T_{am}. For VMD configuration, TPC is defined as

$$TPC = \frac{T_{am}}{T_a} \tag{23}$$

The solution procedure and the flow chart of the calculation were presented in Ref. [54].

3.3. Effect of the coil pitch

In **Figure 16**, it is noticed that the permeate flow rate increases with the increase of the coil pitch to reach their maximum toward the pitch value equaling 32.2 mm and decreases thereafter [44].

It should be noted that when the pitch decreases, the size of the wake also decreases and the empty space between the fibers available for bulk flow is deceased. This leads to a decrease of the feed velocity and the Reynolds number, which causes a decrease of the boundary layer heat transfer coefficient and the permeate flux. However, when the pitch decreases, the fiber exchange surface increases (**Figure 17**). These two variations of permeate flux and fiber exchange surface lead to obtain the optimum pitch, which is 32.2 mm.

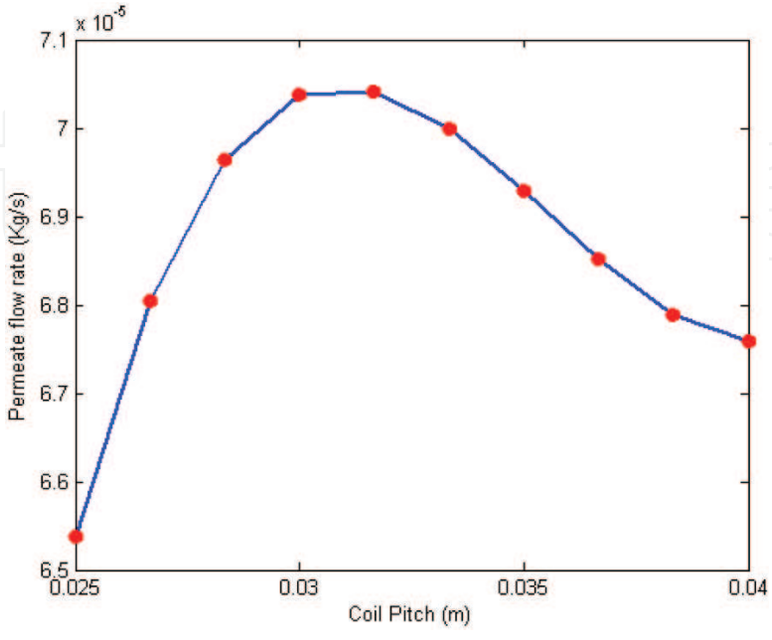

Figure 16. Effect of coil pitch on the permeate flow rate.

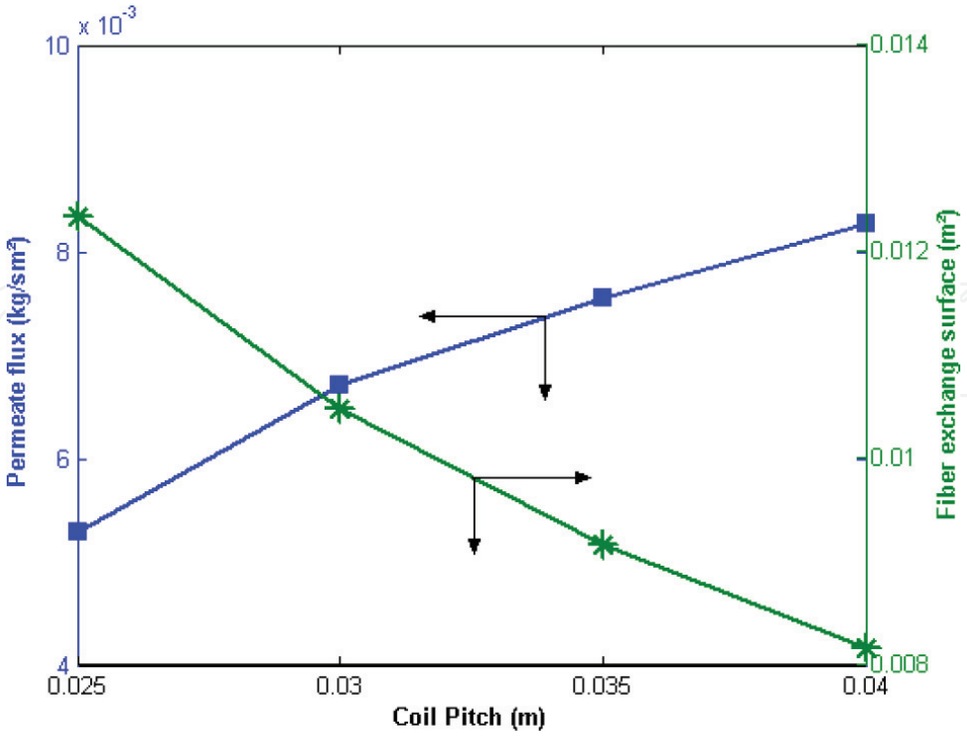

Figure 17. Effect of coil pitch on permeate flux and fiber exchange surface.

3.4. Effect of the distance between fiber and absorber internal wall

In order to optimize the distance between fiber and absorber internal wall, we have used the value of 32.2 mm for the coil pitch. After simulation, the obtained results are shown in **Figure 18**. In this figure, the reliance of the permeate flux on the coil radius is clear. As seen, the permeate flux increases sharply to reach their maximum toward the value of 4.3 mm for the distance between fiber and absorber internal wall (95.7 mm for the coil radius) and decreases thereafter. It is important to say that this decrease is due to the decrease of velocity, which is influenced by the width of the channel between the outside face of fiber and the absorber interior wall. When the value of this width decreases, the effect of channel blockage is remarked. In addition, the parabolic profile of the inlet velocity leads to obtain decreased values of velocity near the absorber interior wall [44].

3.5. Comparison between linear and helical fiber

In order to compare the coil to the linear fibers, we conserve all fiber characteristics and we change only the geometric configuration. In the case of the linear configuration, we are interested by the domain shown in **Figure 19**. Due to symmetry, the modeled domain is reduced to that presented in **Figure 20**.

3.5.1. Effect of fiber configuration in temperature polarization coefficient (TPC).

Figure 21 illustrates the obtained data for the variations of the TPC for the two fiber configurations. These fibers are used in VMD coupled with solar energy in order to increase the temperature of the feed, which flow in the shell-side.

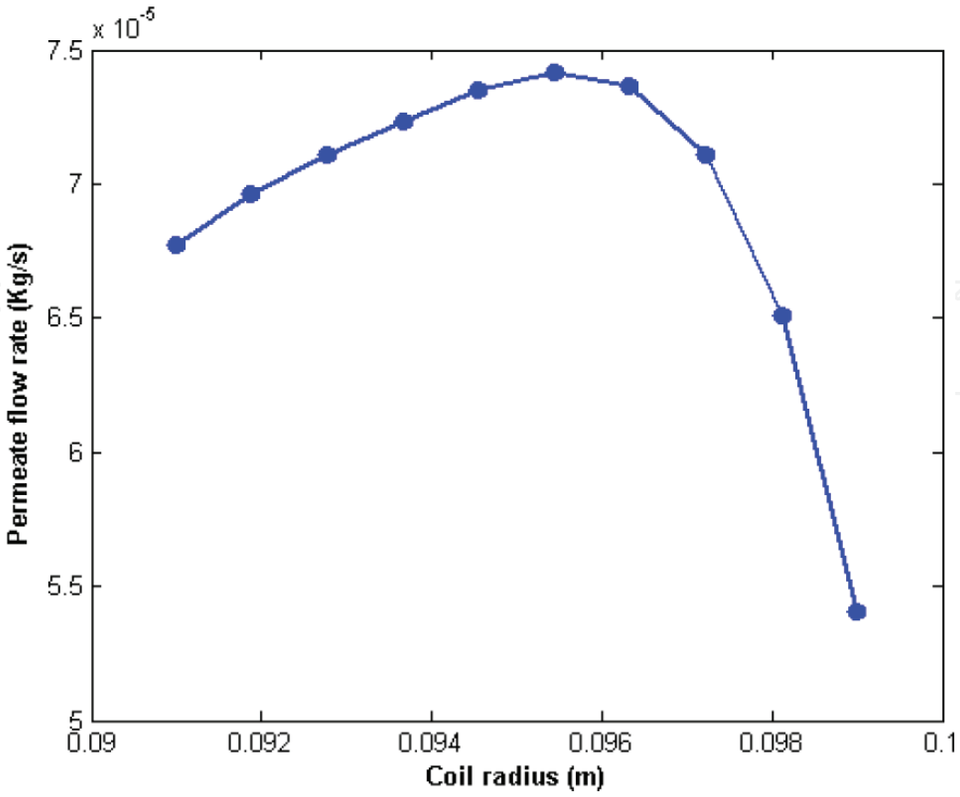

Figure 18. Evolution of permeate flow rate with coil radius.

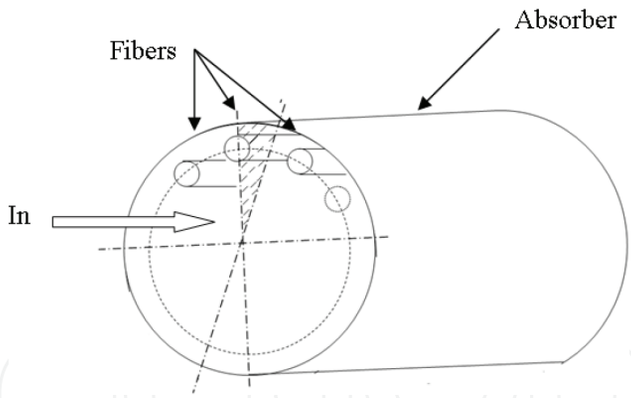

Figure 19. Linear fibers in the solar concentrator absorber.

The inlet feed velocity, in this case, was 3.4×10^{-4} m/s corresponding to a Reynolds number of 68 and the inlet feed temperature was 20°C. According to this figure, two similar evolutions, of the TPC along the module length, were shown for the two fiber configurations. The value of the TPC drops quickly as the module length increases from 0.1 to 0.3 for linear fiber and to 0.2 for helical fiber, and then decreases slowly when the module length increases to 1. For the linear fiber, the TPC decreases first from 0.8688 to 0.8543 and reaches the value of 0.8448 when the module length is 1. Also, for the helical fiber, the decrease, in the first, of the TPC was between 0.9205 and 0.8791 to reach, at the end, the value of 0.8695. However, the TPC of the helical fiber is greater than that of the linear fiber. The improvement factor of the TPC of the helical fiber is in the range of 3–6% compared to the linear one. This improvement can be explained by the fact

http://dx.doi.org/10.5772/67653

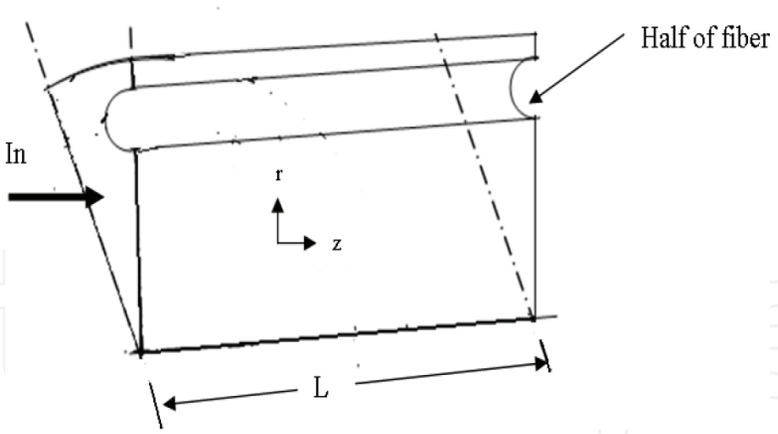

Figure 20. Domain of the study for linear fiber.

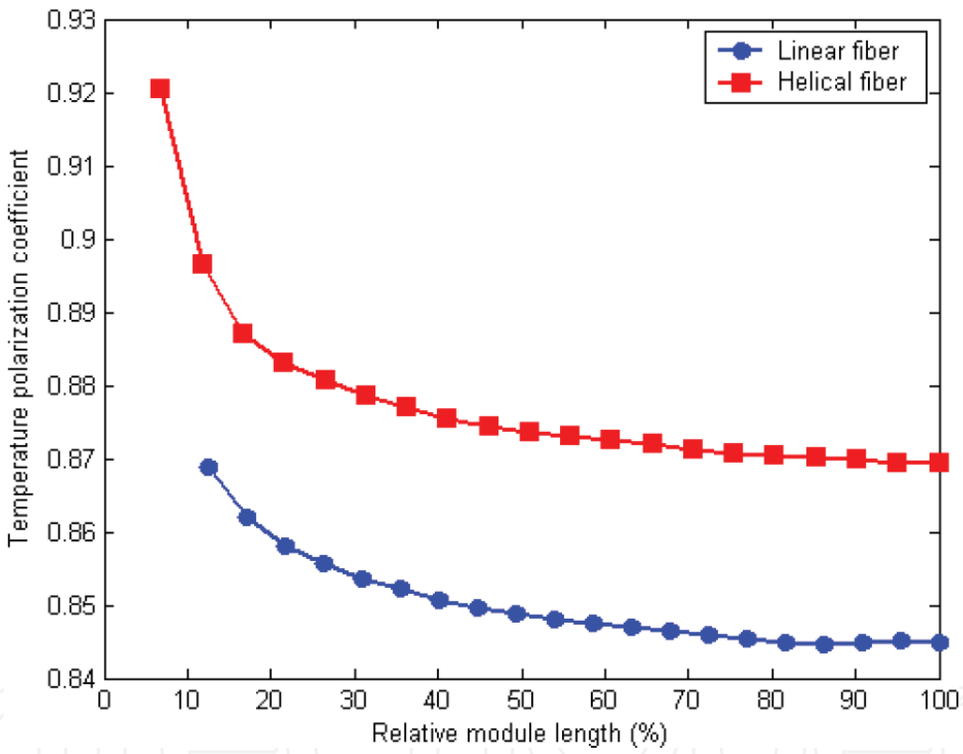

Figure 21. Evolution of temperature polarization coefficient with the relative module length for linear and helical fibers [54].

that for the flow on the shell-side of the helical fiber, a cross flow is developed, of the hot feed in the outside surface of the helical fiber, which allows to enhance the outside heat transfer coefficient. Due to this enhancement, the interface outside membrane temperature (T_{inter}), for the helical fiber, is greater to that for the linear fiber and in the same operating conditions.

3.5.2. Effect of fiber configuration in permeate flow rate

The improvement of T_{inter} leads to an increase of the permeate flow rate for the helical when compared to the linear fiber (**Figure 22**). According to this figure, the evolutions of the permeate flow rate along the module length increase from 2.7×10^{-2} to 3.58×10^{-2} kg/h for the helical

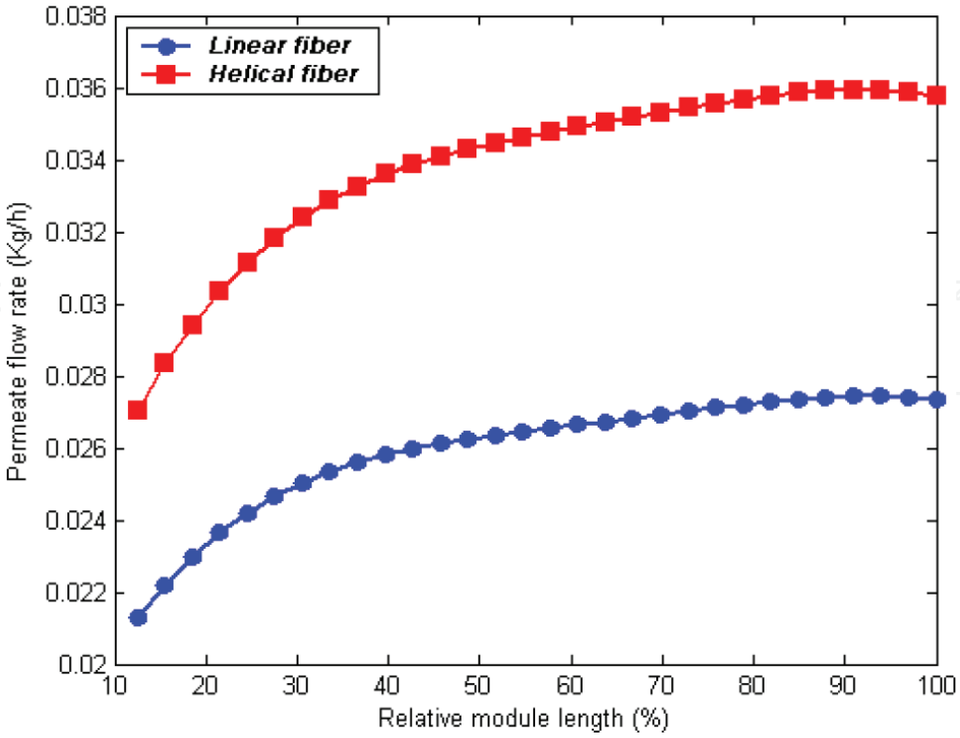

Figure 22. Permeate flow rate versus relative module length for linear and helical fibers [54].

fiber and from 2.12 × 10^{-2} to 2.73 × 10^{-2} kg/h for the linear fiber. In this case, the permeate flow rate for the helical fiber is 0.2685 and 0.21 kg/h for the linear fiber. The improvement factor in this case is about 28%. For the two configurations and along the module, the bulk temperature increases due to the solar rays focused on the exterior absorber wall. This increase in temperature raised the driving force, which is the vapor pressure difference, and the permeate flow rate. The difference between permeate flow rate for the helical and the linear fibers is principally due to the nature of the flow in the fiber outside. In the case of the helical fiber, the cross flow has an important influence on temperature polarization and permeate flow rate. However, cross flow on the shell-side yields a high heat transfer coefficient than parallel flow in the case of linear fiber.

3.5.3. Effect of feed flow rate

The effect of feed flow rate was investigated at the range of 20–60 l/h (Re: 34–102), while the feed temperature was maintained at 20°C. **Figure 23** illustrates the variation of the ratio between helical and linear permeate flow rates with the feed flow rate. It was found that this ratio increases strongly from 20 to 40 l/h and then increases slowly from 1.28 to 1.31 when the feed flow increases from 40 to 60 l/h. It is important to remark that for the solar membrane distillation processes, the amount of energy collected is almost unchangeable for a specific day. For this reason and for our installation, the incident solar radiation is about 800 W/m^2, when the feed flow exceeds 40 l/h, the residence time of the feed in the module decreases and the difference of the bulk temperature between the inlet temperature and the outlet temperature becomes smaller. So optimization of the feed flow rate is an effective way to obtain a high permeate flow rate in VMD coupled with solar.

http://dx.doi.org/10.5772/67653

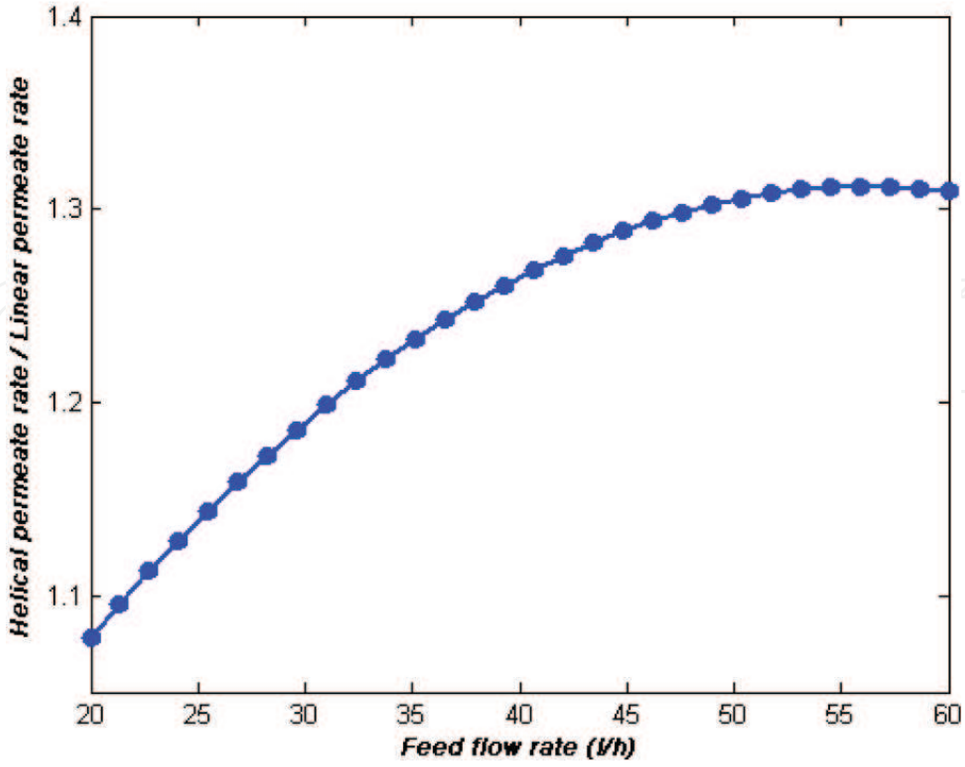

Figure 23. Effects of feed flow rate on the ratio of the helical and linear permeate flow [54].

3.5.4. Effect of inlet feed temperature

To obtain information about the effect of inlet feed temperature on the permeate flow rate, in both fiber configurations, feed temperature was varied in the range of 20–80°C (**Figure 24**) and the feed flow rate was fixed at 40 l/h. Permeate flow rates for both configurations showed an exponential relationship with inlet feed temperature. Although for a given flow rate, feed temperature has a small effect on the Reynolds number. There are only limited changes in viscosity and density. But the enhancement of the permeate flow rate with the inlet feed temperature can be explained by the increase in vapor pressure (Eq. (18)), or driving force (P_{inter}-P_v), with temperature. The helical fiber had a higher permeated flow rate than that of the linear fiber for all temperatures across the entire temperature range. Since the polarization coefficient temperature of the helical fiber was greater than in the linear fiber, T_{inter} in this case becomes close to the feed bulk temperature (T_b). This leads to the evolution of the permeate flow rate between 0.746×10^{-4} and 5.139×10^{-4} kg/s when the inlet feed temperature increases from 20 to 80°C.

3.6. Effect of inlet feed concentration

For our solar vacuum membrane distillation installation, when the inlet feed concentration was varied, the feed temperature and solute concentration rise along the module membrane and influence consequently the permeate flux, J_v, through the membrane. Due to this mass transfer, a temperature and solute concentration gradients are generated in the membrane liquid boundary layer. So, the bulk concentration, C_a, is different from the value at the surface of the membrane, C_{am}.

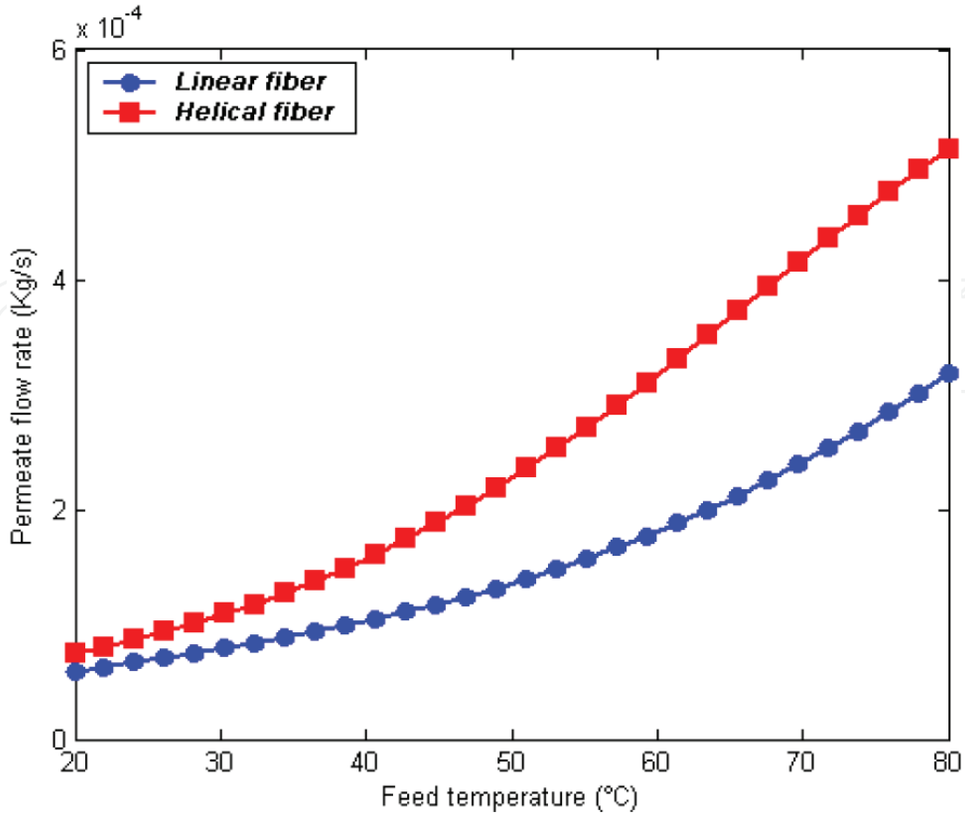

Figure 24. Influence of feed temperature on the permeate flow rate [54].

This concentration can be calculated using the film model and the mass balance across the feed boundary layer as

$$C_{am} = C_a \exp\left(\frac{J_v}{k_c \rho_a}\right) \tag{24}$$

where k_c is the film mass transfer coefficient and ρ_a is the bulk solution density. C_a and C_{am} can be used to calculate the concentration polarization coefficient, CPC, which measure the increase of solute concentration on the membrane surface

$$CPC = \frac{C_{am}}{C_a} \tag{25}$$

Figure 25 shows the effect of the inlet concentration of the feed on the permeate flux. It can be seen that the inlet concentration has a relatively small effect: increasing this concentration from 10 to 300 g/l reduces the permeate flux by only 12%. This moderate effect of the inlet feed concentration on the permeate flux is an advantage for our conception and generally for membrane distillation when it is compared to reverse osmosis system. A drop about 50% is obtained, for this process, when the inlet concentration was varied between 35 and 350 g/l [25].

http://dx.doi.org/10.5772/67653

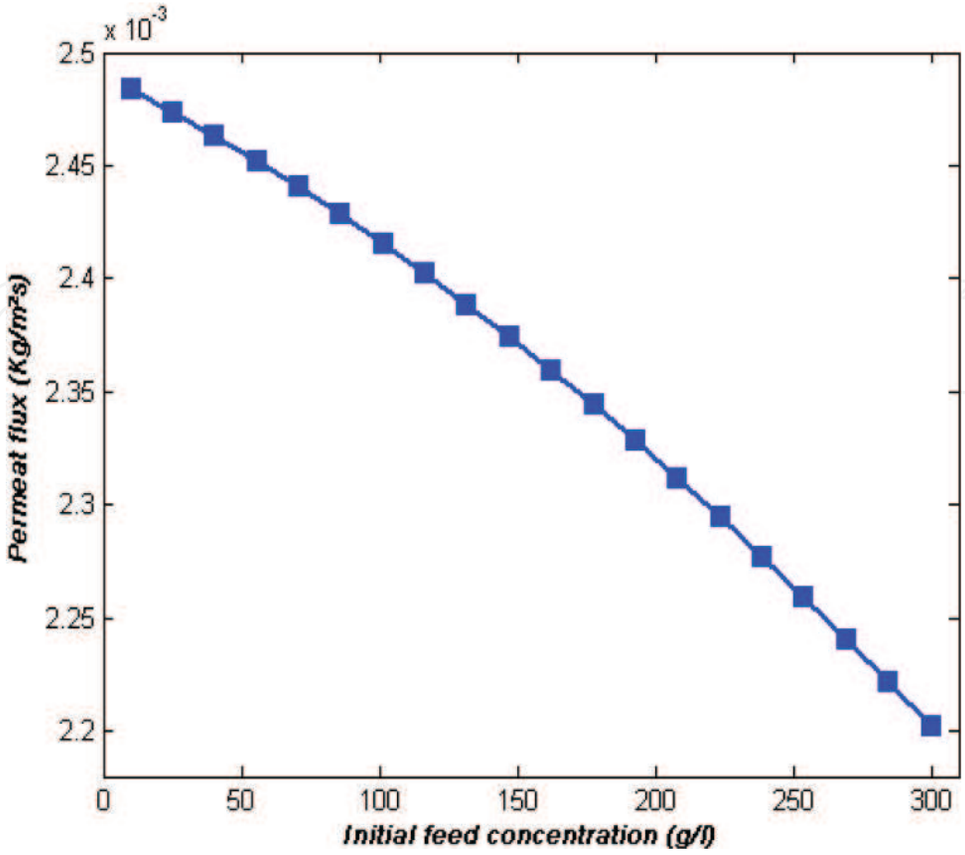

Figure 25. Effect of initial feed salt concentration on the permeate flux [55].

In order to explain the drop of the permeate flux with the increase of the inlet concentration, several phenomena can be advanced. Among these phenomena, we find the temperature polarization, the concentration polarization, and the activity coefficients.

3.6.1. Temperature polarization

The polarization of temperature limits heat transfer into the liquid phase. According to **Figure 26**, the temperature polarization coefficient (TPC) drops from 96.5 to 93.5% when the relative length, of the fiber, rises from 0 to 45%. Beyond this value (45%), the TPC has stabilized around 93.5%. Also, when we have varied the inlet concentration of salt between 10 and 300 g/l, no effect on the TPC was observed.

In this case, the heat transfer was not influenced by the variation of the salt inlet concentration despite the increase in temperature along the membrane module (**Figure 27**) and "T_{am}" rises with the increase of "$T_{a.}$"

3.6.2. Concentration polarization

The concentration polarization limits the mass transfer in the liquid film. In order to investigate the influence of the inlet concentration of salt on the concentration polarization coefficient

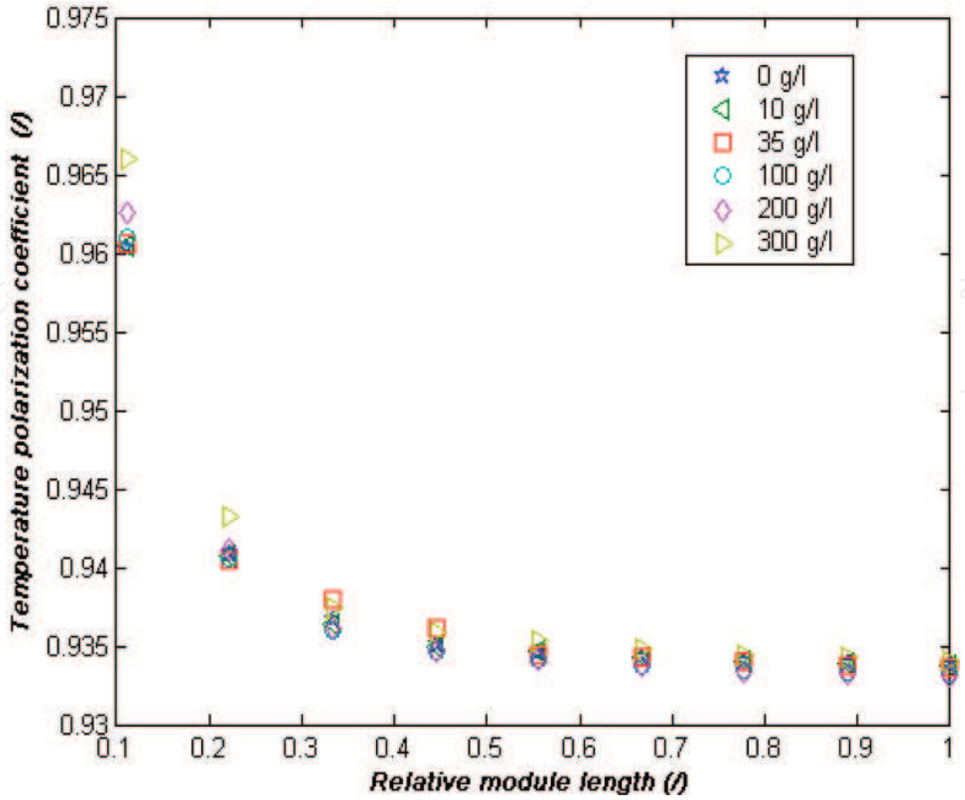

Figure 26. Temperature polarization coefficient as a function of relative module length [55].

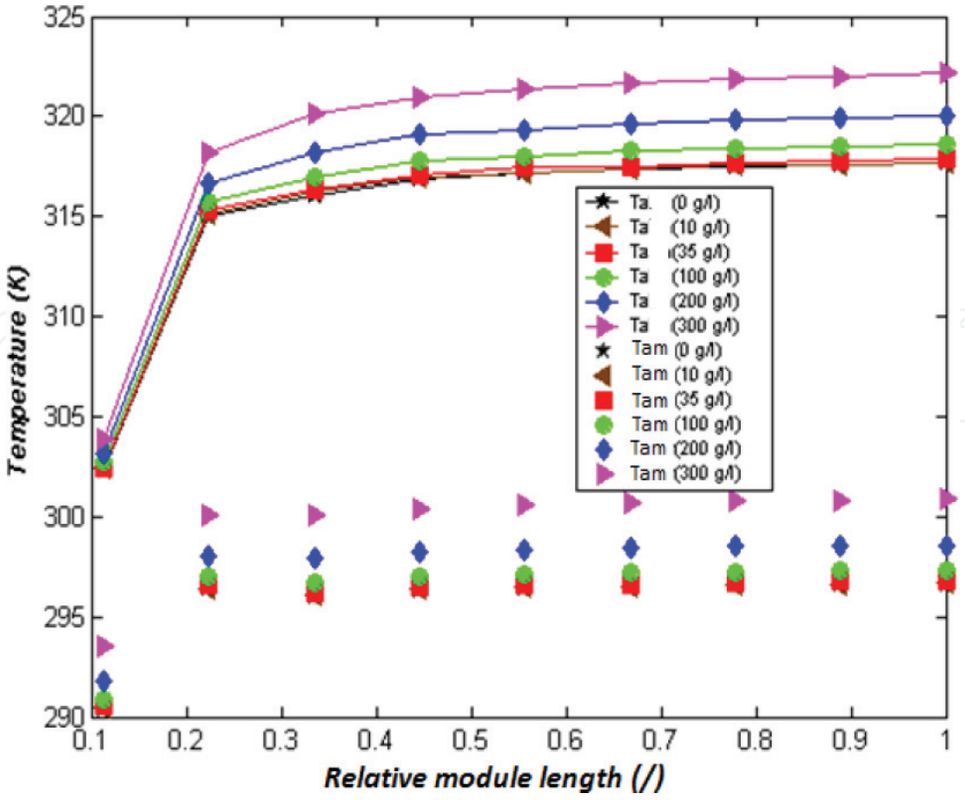

Figure 27. Bulk temperature (T_a) and membrane surface temperature (T_{am}) versus relative module length [55].

(CPC), we have plotted in **Figure 28** the variation of the CPC with the inlet concentration and along the module length.

As seen in this figure, a very small decrease of the CPC with the increase of the inlet concentration of salt is observed. This decrease is due to the decrease of the permeate flux, with the increase of the salt inlet concentration, which leads to the decrease of "C_{am}."

3.6.3. Water activity

The effect of inlet salt concentration on water activity coefficient was examined by varying the inlet salt concentration between 10 and 300g/l. The obtained data shown in **Figure 29** indicate that activity coefficient is almost the same along the module length. This is because of the small value of permeate flow. However, when we varied the inlet concentration, a decrease of 20% for the activity coefficient was remarked. As a consequence, the partial vapor pressure and the driving force of the MD process decrease, which lead to the decrease of the permeate flux (**Figure 30**).

3.7. Effect of solar radiation

In order to explain the relation between the permeate flow rate and the direct solar flux, we have plotted in **Figure 31** the evolution of the permeate flow rate with the direct solar flux. According to this figure, we remarked that the permeate flow rate increases with the increase of the direct solar flux. When the direct solar flux increases, an increasing of the feed temperature is consequently reported.

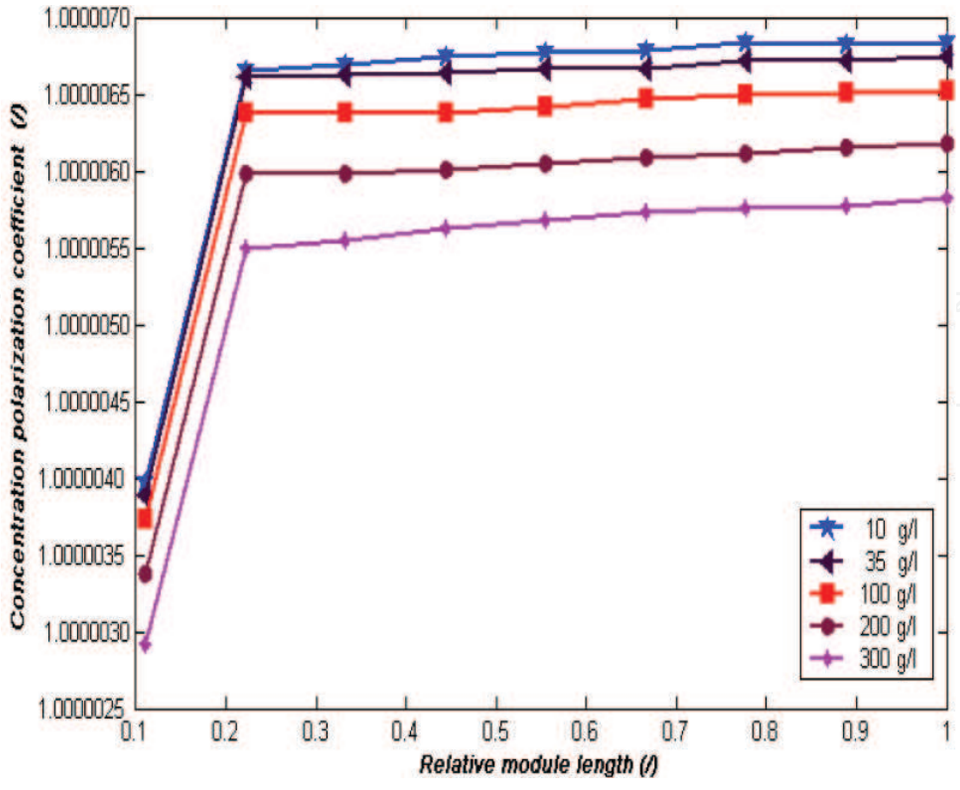

Figure 28. Concentration polarization coefficient versus relative module length [55].

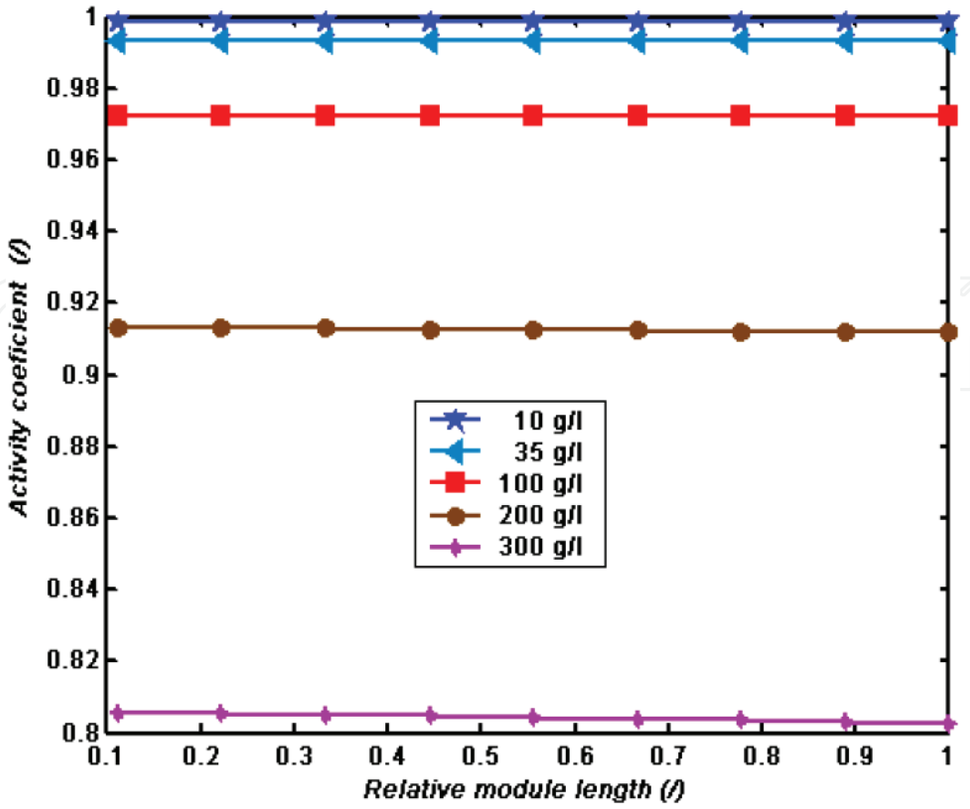

Figure 29. Activity coefficient as a function of relative module length [55].

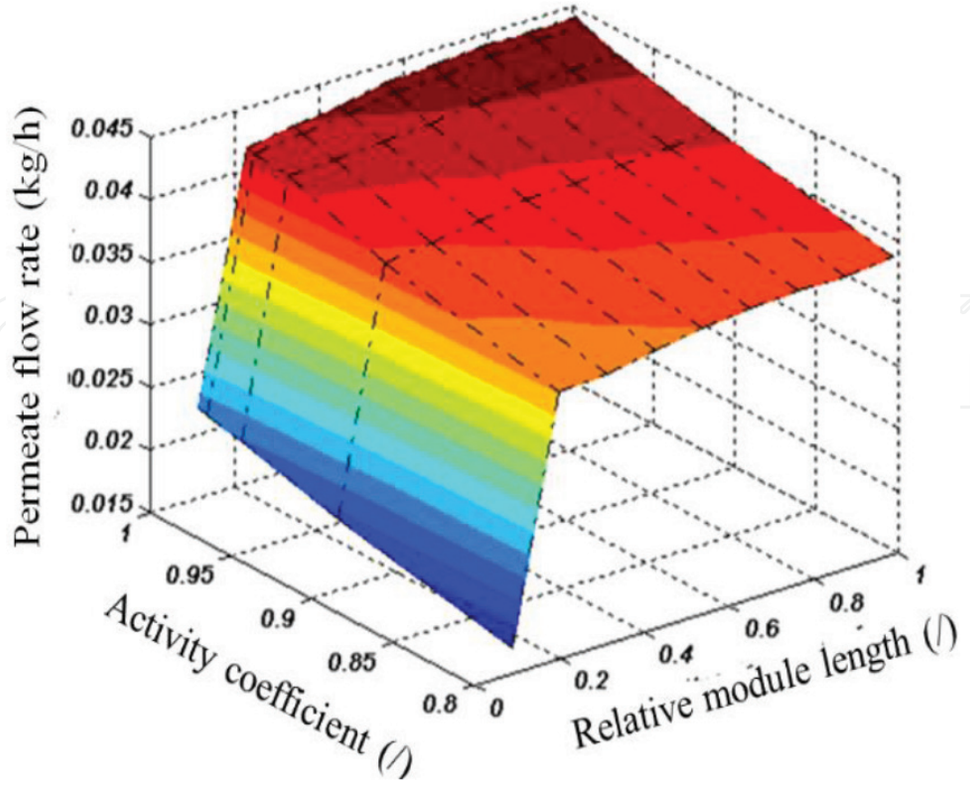

Figure 30. Permeate flow rate as a function of activity coefficient and relative module length [55].

http://dx.doi.org/10.5772/67653

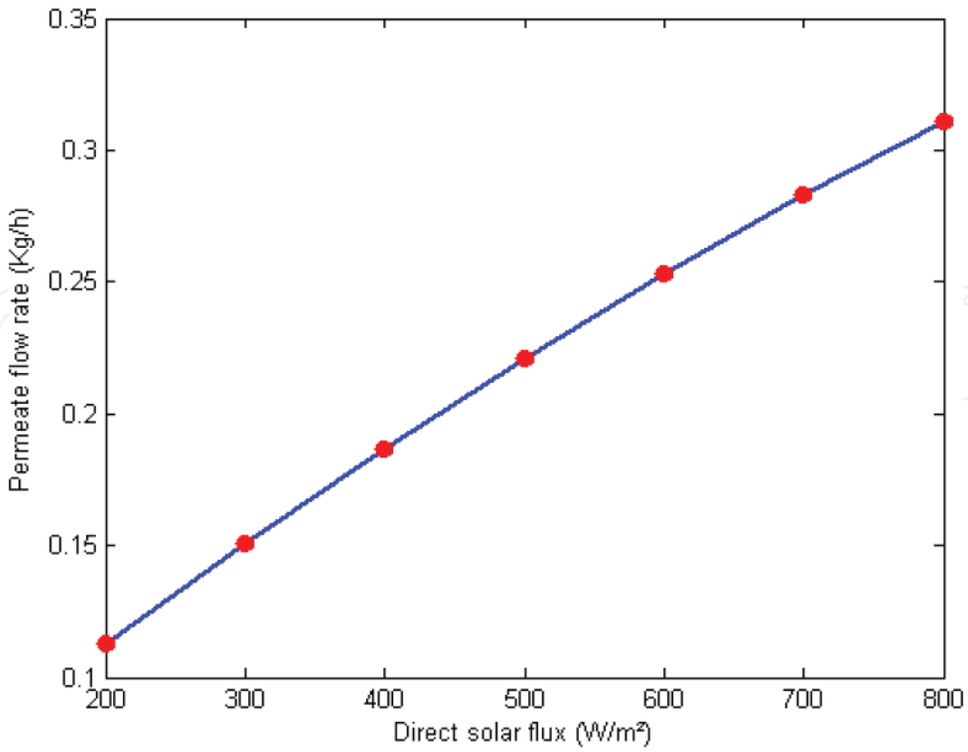

Figure 31. Effect of direct solar flux on the permeate flow rate [56].

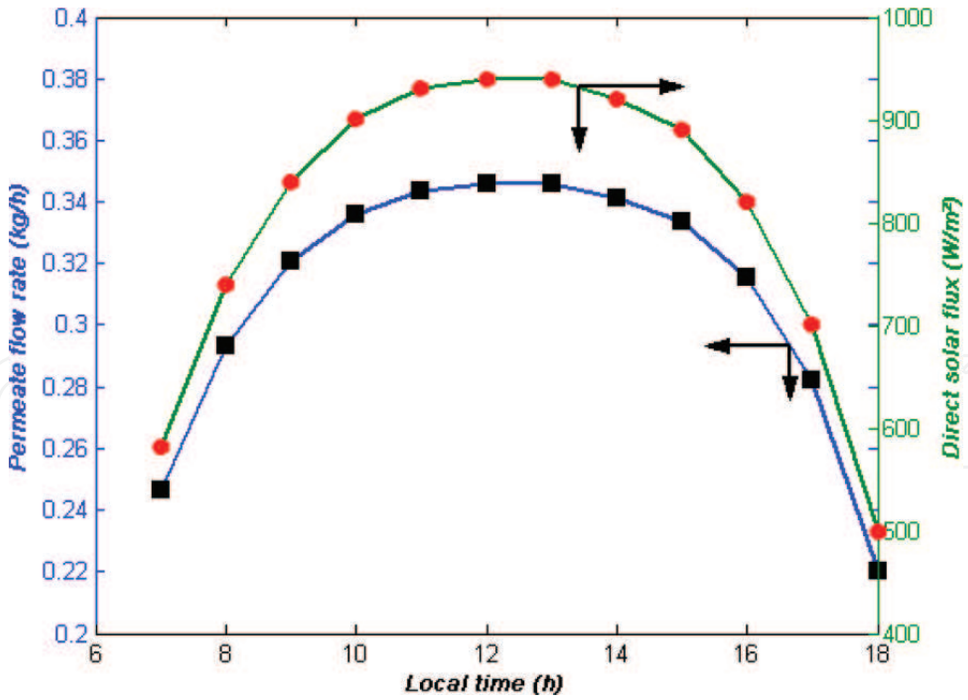

Figure 32. Permeate flow rate and direct solar flux obtained during June 21 [56].

The increase of feed temperature has a small effect on the Reynolds number at a given feed flow rate. The small change is only limited in the density and viscosity of feed. Although the increase of temperature enhances the Reynolds number somewhat, it enhances exponentially

the permeate flux. This effect can be attributed to the higher water vapor sensitivity at high temperatures. This causes the increase of vapor pressure difference or driving force $(P_{H_2O} - Pv)$.

Figure 32 shows the evolution of permeate flow rate and the direct solar flux during June 21, the permeate flow rate increases in the beginning of the day to reach their maximum toward 12 h and decreases thereafter. This evolution is closely linked to the direct solar flux, which is responsible for this production and therefore has a similar evolution.

In order to determine the effect of the initial feed concentration on the permeate flow rate during June 21, we have varied the inlet concentration of salt between 10 and 300 g/l and we have plotted in **Figure 33** the evolutions of the permeate flow rate. As seen in this figure, a decrease of the permeate flow rate with the increase of the inlet feed concentration was remarked.

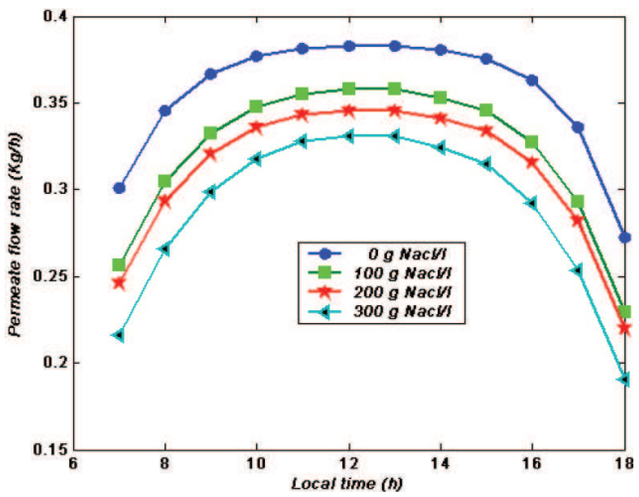

Figure 33. Effect of initial feed salt concentration on the permeate flux during June 21 [56].

4. Conclusions

Distillation process has been in continuous development during the previous decades in order to improve the process efficiency. Therefore, and in order to overcome the disadvantages of the conventional processes, the MD technique has been introduced. This technique has gained much interest, principally, for its lower energy demand and higher rejection factors. In order to improve the MD process performance, many configurations of the hollow fiber have been used. Also and according to some studies, the system efficiencies, of the MD technique, can be improved and its capital cost can be reduced when it is coupled with renewable energy. In this context, we have studied in this chapter the use of the helically coiled fiber in a solar vacuum membrane distillation installation. A mathematical model has been developed in order to describe the evolutions of permeate flow rate with the variation of inlet feed temperature, inlet feed concentration, direct solar flux, and so on. After simulation and comparison between the use of linear fiber and helical-coiled fiber, the results show an enhancement of the temperature polarization coefficient about 6% for the case of the helical fiber. This enhancement leads to obtain an improvement factor by 28% for the helical fiber and to confirm their use for membrane distillation. For the case of the

effect of solar energy on the permeate flow rate, an increase of 264% is remarked for the variation of the direct solar flux from 200 to 800 W/m^2. However, a reduction of 12% for the permeate flux is obtained, when the inlet feed concentration grows from 10 to 300 g/l.

Author details

Adel Zrelli

Address all correspondence to: adel.zrelli@yahoo.fr

1 Environmental, Catalysis and Process Analysis Research Unity, National Engineering School of Gabes, Gabes, Tunisia

2 High Institute of Applied Sciences and Technology of Gabes, University of Gabes, Gabes, Tunisia

References

[1] Lazarova V, Choo K-H, Corne P. Water - energy interactions in water reuse. London: IWA Publishing; 2012. ISBN 13: 9781843395416

[2] Elbeih S F. An overview of integrated remote sensing and GIS for groundwater mapping in Egypt. Ain Shams Engineering Journal. 2015; 6: 1–15. http://dx.doi.org/10.1016/j.asej.2014.08.008

[3] Kummu M, Ward P J, Moel H, Varis O: Is physical water scarcity a new phenomenon? Global assessment of water shortage over the last two millennia. Environmental Research Letters. 2010; 5: 1-10. doi:10.1088/1748-9326/5/3/034006

[4] Pedro-Monzonís M, Solera A, Ferrer J, Estrela T, Paredes-Arquiola J: A Review of Water Scarcity and Drought Indexes in Water Resources Planning and Management. Journal of Hydrology. 2015; 527: 482–493, doi:10.1016/j.jhydrol.2015.05.003

[5] Davis J, O'Grady A P, Dale A, Arthington A, Gell P, Driver P D, Bond N, Casanova M, Finlayson M, Watts R J, Capon S, Nagelkerken I, Tingley R, Fry B, Page T J, Spech A. When trends intersect: the challenge of protecting freshwater ecosystems under multiple land use and hydrological intensification scenarios. Science of the Total Environment. 2015; 534: 65–78. doi:10.1016/j.scitotenv.2015.03.127

[6] Al-Karaghouli A, Kazmerski L L. Renewable Energy Opportunities in Water Desalination. In: Schorr M, editor. Desalination, Trends and Technologies. Rijeka, InTech; 2011. p. 149-184. DOI: 10.5772/14779.ch8

[7] Palenzuela P, Hassan A S, Zaragoza G, Alarcón-Padilla D A. Steady state model for multi-effect distillation case study: Plataforma Solar de Almería MED pilot plant. Desalination. 2014; 337: 31–42. http://dx.doi.org/10.1016/j.desal.2013.12.029

[8] Pelin O. Membrane Distillation: Principle, Advances, Limitations and Future Prospects in Food Industry. In: Zereshki S, editor. Distillation - Advances from Modeling to Applications. Rijeka, InTech; 2012. p. 233-266. DOI: 10.5772/37625. Ch11

[9] Saffarini R B, Summers E K, Arafat H A, Lienhard J H. Economic evaluation of standalone solar powered membrane distillation systems. Desalination. 2012; 299: 55–62. doi:10.1016/j.desal.2012.05.017

[10] Cabassud C, Wirth D. Membrane distillation for water desalination: how to chose an appropriate membrane? Desalination. 2003; 157: 307–314. doi:10.1016/S0011-9164(03)00410-7

[11] Khayet M, Matsuura T. Membrane distillation principles and applications. UK: Elsevier; 2011. ISBN: 978-0-444-53126-1

[12] Bataineh K M. Multi-effect desalination plant combined with thermal compressor driven by steam generated by solar energy. Desalination. 2016; 385: 39–52. doi:10.1016/j.desal.2016.02.011

[13] Sharaf M A, Nafey A S, García-Rodríguez L. Exergy and thermo-economic analyses of a combined solar organic cycle with multi effect distillation (MED) desalination process. Desalination. 2011; 272: 135–147. doi:10.1016/j.desal.2011.01.006

[14] Al-Karaghouli A, Renne D, Lawrence L. Kazmerski L L. Solar and wind opportunities for water desalination in the Arab regions. Renewable and Sustainable Energy Reviews. 2009; 13: 2397–2407. doi:10.1016/j.rser.2008.05.007

[15] Carayannis E G. Creating a sustainable social ecology using technology-driven solutions, 1st ed. USA: IGI Global; 2013. ISBN-13: 978-1466636132

[16] Bruggen B V, Vandecasteele C. Distillation vs. membrane filtration: overview of process evolutions in seawater desalination evolutions in seawater desalination. Desalination. 2002; 143: 207–218. doi:10.1016/S0011-9164(02)00259-X

[17] Gude V G. Geothermal source potential for water desalination – current status and future perspective. Renewable and Sustainable Energy Reviews. 2016; 57: 1038–1065. doi:10.1016/j.rser.2015.12.186

[18] Charcosset C. A review of membrane processes and renewable energies for desalination. Desalination. 2009; 245: 214–231. doi:10.1016/j.desal.2008.06.020

[19] AlMadani H M N. Water desalination by solar powered electrodialysis process. Renewable Energy. 2003; 28: 1915–1924. doi:10.1016/S0960-1481(03)00014-4

[20] Abdel-Aal E A, Farid M E, Hassan F S M, Adila E M. Desalination of Red Sea water using both electrodialysis and reverse osmosis as complementary methods. Egyptian Journal of Petroleum. 2015; 24: 71–75. http://dx.doi.org/10.1016/j.ejpe.2015.02.007

[21] Abdallaha S, Abu-Hilala M, Mohsen M S. Performance of a photovoltaic powered reverse osmosis, system under local climatic conditions. Desalination. 2005; 183: 95–104. doi:10.1016/j.desal.2005.03.030

[22] Eshoul N M, Agnew B, Al-Weshahi M A, Atab M S. Exergy analysis of a two-pass reverse osmosis (RO) desalination unit with and without an energy recovery turbine (ERT) and pressure exchanger (PX). Energies. 2015; 8: 6910–6925. doi:10.3390/en8076910

[23] Ali S M, Chakraborty A. Adsorption assisted double stage cooling and desalination employing silica gel + water and AQSOA-Z02 + water systems. Energy Conversion and Management. 2016; 117: 193–205. http://dx.doi.org/10.1016/j.enconman.2016.03.007

[24] Khawaji A D, Kutubkhanah I K, Wie J-M. Advances in seawater desalination technologies. Desalination. 2008; 221: 47–69. doi:10.1016/j.desal.2007.01.067

[25] Al-Obaidania S, Curcio E, Macedonio F, Di Profio G, Al-Hinai H, Drioli E. Potential of membrane distillation in seawater desalination: thermal efficiency sensitivity study and cost estimation. Journal of Membrane Science. 2008; 323: 85–98. doi:10.1016/j.memsci.2008.06.006

[26] Fard A K, Rhadfi T, Khraisheh M, Atieh M A, Khraisheh M, Hilal N. Reducing flux decline and fouling of direct contact membrane distillation by utilizing thermal brine from MSF desalination plant. Desalination. 2016; 379: 172–181. http://dx.doi.org/10.1016/j.desal.2015.11.004

[27] Boo C, Lee J, Elimelech M. Engineering surface energy and nanostructure of microporous films for expanded membrane distillation applications. Environmental Science & Technology. 2016. doi:10.1021/acs.est.6b02316

[28] Qtaishat M R, Banat F. Desalination by solar powered membrane distillation systems. Desalination. 2013; 308: 186–197. doi:10.1016/j.desal.2012.01.021

[29] Janajreh I, Suwwan D, Hashaikeh R. Theoretical and experimental study of direct contact membrane distillation. Desalination and Water Treatment. 2016; 57(33): 15660–15675. http://dx.doi.org/10.1080/19443994.2015.1131198

[30] Hassan M I, Brimmo A T, Swaminathan J, Lienhard J H, Arafat H A. A new vacuum membrane distillation system aspirator: concept modeling and optimization using an aspirator. Desalination and Water Treatment. 2016; 57(28): 12915–12928. http://dx.doi.org/10.1080/19443994.2015.1060902

[31] Cheng D, Gong W, Li N. Response surface modeling and optimization of direct contact membrane distillation for water desalination. Desalination. 2016; 394: 108–122. http://dx.doi.org/10.1016/j.desal.2016.04.029

[32] Moudjeber D E, -Aguirre A R, Ugarte-Judge D, Mahmoudi H, Zaragoza G: Solar desalination by air-gap membrane distillation: a case study from Algeria. Desalination and Water Treatment. 2016: 57; 22718-22725; http://dx.doi.org/10.1080/19443994.2016.113910

[33] Huayan C, Chunrui W, Yue J, Xuan W, Xiaolong L. Comparison of three membrane distillation configurations and seawater desalination by vacuum membrane distillation. Desalination and Water Treatment. 2011; 28: 321–327. doi:10/5004/dwt.2011.1605

[34] Simone S, Figoli A, Criscuoli A, Carnevale M C, Rosselli A, Drioli E. Preparation of hollow fiber membranes from PVDF/PVP blends and their applications in VMD. Journal of Membrane Science. 2010; 364: 291–232. doi:10.1016/j.memsci.2010.08.013

[35] Safavi M., Toraj M. High-salinity water desalination using VMD. Chemical Engineering Journal. 2009; 149: 191–195. doi:10.1016/j.cej.2008.10.021

[36] Li G-P, Zhang L-Z. Investigation of a solar energy driven and hollow fiber membrane-based humidification–dehumidification desalination system. Applied Energy. 2016; 177: 393–408. http://dx.doi.org/10.1016/j.apenergy.2016.05.113

[37] Banat F, Jwaied N. Economic evaluation of desalination by small-scale autonomous solar-powered membrane distillation units. Desalination. 2008; 220: 566–573. doi:10.1016/j.desal.0000.00.000

[38] Teoh M M, Bonyadi S, Chung T-S. Investigation of different hollow fiber module designs for flux enhancement in the membrane distillation process. Journal of Membrane Science. 2008; 311: 371–379. doi:10.1016/j.memsci.2007.12.054

[39] Yang X, Wang R, Fane A G. Novel designs for improving the performance of hollow fiber membrane distillation modules. Journal of Membrane Science. 2011; 384: 52–62. doi:10.1016/j.memsci.2011.09.007

[40] Yang X, Yu H, Wang R, Fane A G. Optimization of microstructured hollow fiber design for membrane distillation applications using CFD modelling. Journal of Membrane Science. 2012; 421–422: 258–270. http://dx.doi.org/10.1016/j.memsci.2012.07.022

[41] Qu D, Zhou T, Ma W, Peng Z, Li Z, Qin M. Comparison of hollow fiber module designs in membrane distillation process employed lumen-side and shell-side feed. Desalination and Water Treatment. 2016; 57(17): 7700–7710. http://dx.doi.org/10.1080/19443994.2015.1049561

[42] Mallubhota H, Hoffman S, Schidt M, Vente J, Belfort G. Flux enhancement during dean vortex tubular membrane nanofiltration. 10. Design, construction, and system characterization. Journal of Membrane Science. 1998; 141: 183–195. doi:10.1016/S0376-7388(98)00255-5

[43] Nagase K, Kohori F, Sakai K, Nishide H. Rearrangement of hollow fibers for enhancing oxygen transfer in an artificial gill using oxygen carrier solution. Journal of Membrane Science. 2005; 254: 207–217. doi:10.1016/j.memsci.2005.01.008

[44] Zrelli A, Chaouchi B, Gabsi S. Simulation of vacuum membrane distillation coupled with solar energy: optimization of the geometric configuration of a helically coiled fiber. Desalination and Water Treatment. 2011; 36: 41–49. doi:10.5004/dwt.2011.1831

[45] Bird R B, Stewart E W, lightfoot E N. Transport phenomena, 2nd ed. New York: John Wiley & Sons, Inc.; 2002.

[46] Mericq J P, Laborie S, Cabassud C. Vacuum membrane distillation of seawater reverse osmosis brines. Water Research. 2010; 44: 5260–5273. doi:10.1016/j.watres.2010.06.052

[47] Chaouchi B, Zrelli A, Gabsi S. Desalination of brackish water by means of a parabolic solar concentrator. Desalination. 2007; 217: 118–126. doi:10.1016/j.desal.2007.02.009

[48] Wirth D, Cabassud C. Water desalination using membrane distillation: comparison between inside/out and outside/in permeation. Desalination. 2002; 147: 139–145. doi:10.1016/S0011-9164(02)00601-X

[49] Izquierdo M A, Jonsson G. Factors affecting flux and ethanol separation performance in vacuum membrane distillation (VMD). Journal of Membrane Science. 2003; 214: 113–130. http://dx.doi.org/10.1016/S0376-7388(02)00540-9

[50] Mengual J I, Khayet M, Godino M P: Heat and mass transfer in vacuum membrane distillation. International Journal of Heat and Mass Transfer. 2004; 47: 865–875. doi:10.1016/j.ijheatmasstransfer.2002.09.001

[51] Banat F, Jumah R, Garaibeh M. Exploitation of solar energy collected by solar stills for desalination by membrane distillation. Renewable Energy. 2002; 25: 293–305. http://dx.doi.org/10.1016/S0960-1481(01)00058-1

[52] Salimpour M R. Heat transfer characteristics of a temperature-dependent-property fluid in shell and coiled tube heat exchangers. International Communications in Heat and Mass Transfer. 2008; 35: 1190–1195. http://dx.doi.org/10.1016/j.icheatmasstransfer.2008.07.002

[53] Salimpour M R. Heat transfer coefficients of shell and coiled tube heat exchangers. Experimental Thermal and Fluid Science. 2009; 33: 203–207. http://dx.doi.org/10.1016/j.expthermflusci.2008.07.015

[54] Zrelli A, Chaouachi B, Gabsi S. Simulation of a solar thermal membrane distillation: comparison between linear and helical fibers. Desalination and Water Treatment. 2014; 52(7–9): 1683–1692. doi:10.1080/19443994.2013.807033

[55] Zrelli A, Chaouachi B, Gabsi S. Impact of the feed concentration on the permeate flux of the solar vacuum membrane distillation equipped with helically coiled fibers. In: Proceeding of IEEE Renewable Energy Congress (IREC), 2014 5th International. doi:10.1109/IREC.2014.6827014

[56] Zrelli A, Chaouachi B, Gabsi S. Use of solar energy for desalination by membrane distillation installation equipped with helically coiled fibers. In: Proceeding of IEEE Renewable Energy Congress (IREC), 2015 6th International. doi:10.1109/IREC.2015.7110893

IntechOpen